Title
Nano-Engineering of Silicate Glasses Toward Improved Functionalities

Author
Yu, Yingtian

Publication Date
2017

Peer reviewed|Thesis/dissertation

UNIVERSITY OF CALIFORNIA

Los Angeles

Nano-Engineering of Silicate Glasses Toward Improved Functionalities

A dissertation submitted in partial satisfaction of the requirements for the degree

Doctor of Philosophy

in Civil Engineering

by

Yingtian Yu

2017

ABSTRACT OF THE DISSERTATION

Nano-Engineering of Silicate Glasses Toward Improved Functionalities

by

Yingtian Yu

Doctor of Philosophy in Civil Engineering

University of California, Los Angeles, 2017

Professor Mathieu Bauchy, Chair

Glasses can be made of virtually all the elements of the periodic table, provided that a melt is cooled fast enough from the liquid state. The number of possible glass compositions is virtually infinite. Although such a large compositional space offers limitless opportunities to develop novel glasses with improved functionalities, it also comes with some challenges, since the large number of possible compositions render traditional “trial and error” Edisonian approaches poorly efficient. As a goal of this thesis, overcoming the limit of empirical approaches of glass design requires the development of accurate and transferable predictive models linking glasses’ composition and structure to their macroscopic property, is crucially important to the glass science community.

The dissertation of Yingtian Yu is approved.

Gaurav N. Sant

Laurent Pilon

Scott J. Brandenberg

Mathieu Bauchy, Committee Chair

University of California, Los Angeles

2017

Table of Content

Table of Figure and Table

Vita

- Education:

B.S. Physics, Michigan State University
M.S. Mechanical Engineering, Michigan State University

- Publication:

1. Yu, Y. *et al.* Stretched exponential relaxation of glasses at low temperature. *Phys. Rev. Lett.* **115,** 165901 (2015).

2. Yu, Y., Wang, B., Wang, M., Sant, G. & Bauchy, M. Reactive Molecular Dynamics Simulations of Sodium Silicate Glasses—Toward an Improved Understanding of the Structure. *Int. J. Appl. Glass Sci.* **8,** 276–284 (2017).

3. Yu, Y., Wang, B., Wang, M., Sant, G. & Bauchy, M. Revisiting silica with ReaxFF: towards improved predictions of glass structure and properties via reactive molecular dynamics. *J. Non-Cryst. Solids* **443,** 148–154 (2016).

4. Yu, Y., Wang, B., Lee, Y. J. & Bauchy, M. Fracture toughness of silicate glasses: Insights from molecular dynamics simulations. *MRS Online Proc. Libr. Arch.* **1757,** (2015).

5. Wang, M. *et al.* Ion exchange strengthening and thermal expansion of glasses: Common origin and critical role of network connectivity. *J. Non-Cryst. Solids* **455,** 70–74 (2017).

6. Wang, B., Yu, Y., Wang, M., Mauro, J. C. & Bauchy, M. Nanoductility in silicate glasses is driven by topological heterogeneity. *Phys. Rev. B* **93,** 064202 (2016).
7. Wang, B., Yu, Y., Pignatelli, I., Sant, G. & Bauchy, M. Nature of radiation-induced defects in quartz. *J. Chem. Phys.* **143,** 024505 (2015).

8. Wang, B., Yu, Y., Lee, Y. J. & Bauchy, M. Intrinsic nano-ductility of glasses: the critical role of composition. *Front. Mater.* **2,** 11 (2015).

9. Wang, B. *et al.* Irradiation-induced topological transition in SiO 2: Structural signature of networks' rigidity. *J. Non-Cryst. Solids* **463,** 25–30 (2017).

10. Pignatelli, I. *et al.* Direct experimental evidence for differing reactivity alterations of minerals following irradiation: the case of calcite and quartz. *Sci. Rep.* **6,** (2016).

11. Huang, J. *et al.* Electronic Origin of Doping-Induced Enhancements of Reactivity: Case Study of Tricalcium Silicate. *J. Phys. Chem. C* **119,** 25991–25999 (2015).

12. Bauchy, M. *et al.* Fracture toughness anomalies: Viewpoint of topological constraint theory. *Acta Mater.* **121,** 234–239 (2016).

- List of Conference Presentations:

1. Presentation on “Application of ReaxFF to glassy silica”, Glass & Optical Material Division annual meeting 2015, The American Ceramic Society.

2. Presentation on “Composition-Hardness Relation in Silicate Glasses”, Glass & Optical Material Division annual meeting 2016, The American Ceramic Society.

3. Presentation on “Improved Description of Structure of Silica and Silicate Glasses through Reactive Molecular Dynamics Simulations”, Glass & Optical Material Division annual meeting 2017, The American Ceramic Society.

4. Presentation on “Silica Reactivity is Driven by the Surface Topology”, Glass & Optical Material Division annual meeting 2017, The American Ceramic Society.

5. Invited presentation on “Stretched Exponential Relaxation of Glasses at Low Temperatures”, Glass & Optical Material Division annual meeting 2017, The American Ceramic Society.

6. Poster on “Engineering Radiation-Resistant Materials from the Atomic Scale”, Glass & Optical Material Division annual meeting 2015, The American Ceramic Society.

7. Poster on “Effect of Surface Topology on Silica Reactivity: Insights from Reactive Molecular Dynamics”, Glass & Optical Material Division annual meeting 2016, The American Ceramic Society.

8. Poster on “Hardness of Silicate Glasses: Origin of the Mixed Modifier Effect”, Glass & Optical Material Division annual meeting 2017, The American Ceramic Society.

Part I. Introduction and Motivation of the Work

Glasses can be made of virtually all the elements of the periodic table, provided that a melt is cooled fast enough from the liquid state. In addition, unlike crystalline materials that have fixed compositions, glasses do not have to obey any given stoichiometry, namely, its constituents can be present in variable proportions. For all these reasons, the number of possible glass compositions is virtually infinite, even for a given family of materials (e.g., modified aluminosilicate glasses). Although such a large compositional space offers limitless opportunities to develop novel glasses with improved functionalities, it also comes with some challenges, since the large number of possible compositions render traditional “trial and error” Edisonian approaches poorly efficient. Such conventional methods often require hundreds of thousands of experiments or large amounts of simulations, which often ends up in only a narrow composition range being explored. Overcoming the limit of empirical approaches of glass design requires the development of accurate and transferable predictive models linking glasses’ composition and structure to their macroscopic property. This is the primary goal of this thesis.

Although several properties of glasses can be relevant for various applications, we focus in the following on understanding the effect of composition and structure on:

1) Chemical reactivity in aqueous solutions, which characterizes the durability of glasses when exposed to water or humid conditions,
2) Hardness, which characterizes the resistance of glasses to permanent deformations, and,

3) Relaxation, which arises from the intrinsic non-equilibrium nature of glasses.

Studying composition–mechanical properties relationships is important for various applications, including smartphone screens. It is complicated by the fact that even simple properties like the stiffness often exhibit some non-linearity with respect to composition. In addition, existing models usually lack a physical basis or are limited to a narrow range of compositions. Understanding glass reactivity in aqueous conditions is critical for various applications, including bioactive glasses and nuclear waste immobilization glasses. The development of such models is traditionally complicated by a lack of knowledge regarding the mechanism of glass' reactivity and dissolution. Finally, understanding, predicting, and controlling glass relaxation is important for the manufacturing of large display glasses for LCD or OLED screens, as any small variation in the dimension of the glass can result in undesirable pixel misalignments.

To achieve these goals, our approach relies on two main ingredients:

1) Atomistic molecular dynamics (MD) simulations, which can be used to access the atomic-scale details of glasses, which is usually "invisible" to most experimental techniques.
2) Topological constraint theory (TCT), which reduces complex atomic networks into simpler mechanical trusses, which permits to describe the important role of the atomic topology on glasses' macroscopic properties while filtering out less relevant structural details.

As a key novelty, the present thesis applies for the first time the reactive potential ReaxFF to glasses. Unlike conventional classical force-field used for molecular dynamics, ReaxFF can handle charge transfers among atoms and adjust the energy of interaction among atoms based on their local environments, which makes it possible to study reactivity as well as the role of coordination defects in glasses. In turn, ReaxFF is significantly less computationally demanding than quantum-based *ab initio* approaches. As such, reactive potential like ReaxFF open new possibilities in the modeling of glasses and come with great promises for the future.

Part II. Background: Molecular Dynamics and Topological Constraint Theory

Molecular dynamics (MD) in general and two specific types (classical MD & reactive MD) are introduced in detail first in this Part. All the simulation methods that are later used are introduced. Above all, molecular dynamics (MD) in general is explained first.

(i) Introduction to MD in general (specific types includes such as classical MD and reactive MD).

(ii) Classical MD, used in mechanical-composition relation.

(iii) Reactive MD, used in reactivity-composition relation.

Topological constraint theory (TCT) is introduced thereafter.

2.1 Introduction of Molecular Dynamics (MD)

Molecular dynamics (MD) numerically integrates Newton's equations of motions for a system of particles. Starting with an initial configuration, the system is equilibrated before various time-averaged properties can be measured. Here is a summary of the four steps that MD follows to iterate through time.

(i) Start with a particle configuration, with known positions and velocities.

(ii) Calculate the forces on all particles with empirical potential.

(iii) Calculate the acceleration of all particles with Newton's second law.

(iv) Integrate Newton's equations of motions to obtain new positions and velocities, then return to step (i).

Following diagram in Figure 1 illustrates the iteration process that allows molecular dynamics to move particles through time.

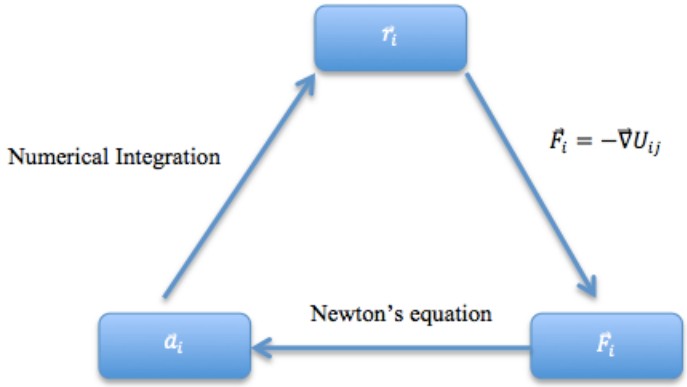

Figure 1: Diagram of the iterative process used as the basis of molecular dynamics simulations.

2.1.1 Classical MD—Jakse potential

Classical MD is an efficient and widely used way to explore non-reactive systems. With a fixed atom charge, classical MD maintains focus on atomic structure therefore save valuable computational time.

Potential and parameterization

Jakse potential is the most popular potential used for CAS glass system. The interatomic potential is in the following form:

$$\mathbf{U_{ij}(r_{ij}) = \frac{q_i q_j}{4\pi\varepsilon r_{ij}} + A_{ij}\exp\left(\frac{\sigma_{ij}-r_{ij}}{\rho_{ij}}\right) - \frac{C_{ij}}{r_{ij}^6} + D_{ij}/r_{ij}^8} \qquad \textbf{Equation 1}$$

where i and j are atom numbers, r_{ij} is the distance between atom i and atom j. A_{ij}, σ_{ij}, ρ_{ij} and D_{ij} are the parameters of the potential. Recently Jakse re-parameterize the potential based on the ab initio calculation[1]. The new sets of parameters are tabulated in the following table. In order to better understand the role of inter-atomic potential on glass property and study the relative quality between different potentials, Matsui's potential is also studied consistently with Jakse potential. The following two tables (

Table I and Table II) are the parameterizations of both Jakse and Matsui potentials both take the form of $\mathbf{U_{ij}(r_{ij}) = \frac{q_i q_j}{4\pi\varepsilon r_{ij}} + A_{ij} exp\left(\frac{\sigma_{ij}-r_{ij}}{\rho_{ij}}\right) - \frac{C_{ij}}{r_{ij}^6} + D_{ij}/r_{ij}^8}$ Equation 1.

Table I: Two-body parameters for Matsui's potential.

Pair	A_{ij}(kcal/m	ρ_{ij}(Å	σ_{ij}(Å)	C_{ij}(kcal/mol	D_{ij}(kcal/mol
O–O	0.275993	0.27	3.643	1962.231	0.0
O–Si	0.160996	0.16	2.5419	1067.63	0.0
O–Al	0.171995	0.17	2.6067	797.366	0.0
O–	0.177995	0.17	2.9935	974.51	0.0
Si–Si	0.045998	0.04	1.4408	580.887	0.0
Si–Al	0.056998	0.05	1.5056	433.839	0.0
Si–	0.062998	0.06	1.8924	530.221	0.0
Al–Al	0.067998	0.06	1.5704	324.01526	0.0
Al–	0.073998	0.07	1.9572	395.9991	0.0
Ca–	0.079998	0.08	2.344	483.975	0.0

Table II: Two body parameters for Jakse potential.

Pair	A_{ij}(kcal/m	ρ_{ij}(Å)	σ_{ij}(Å)	C_{ij}(kcal/mol	D_{ij}(kcal/mol
O–O	0.276344	0.26	3.64	1959.372	0.0
O–Si	0.16120	0.15	2.54	1066.0667	0.0
O–Al	0.172715	0.16	2.60	796.2097	0.0
O–Ca	0.17732	0.17	2.99	973.0907	0.0
Si–Si	0.027634	0.04	1.44	580.030	0.0
Si–Al	0.057571	0.05	1.50	433.2063	0.0
Si–Ca	0.062177	0.06	1.89	529.445489	0.0
Al–Al	0.066783	0.06	1.57	323.548	0.0
Al–Ca	0.073691	0.07	1.95	395.425476	0.0
Ca–	0.080600	0.08	2.34	483.27068	0.0

2.1.2 Reactive potential—ReaxFF

Unlike classical MD where charges are fixed for atoms, ReaxFF dynamically attribute charges among atoms, hence able to model chemical reaction. In addition, it is an extremely efficient method which is about 1 million times faster than *ab initio* quantum molecular dynamics calculations.

Introduction to ReaxFF

ReaxFF[2] is a reactive force field, based on a dynamic bond order, which is determined on the fly with respect to the instantaneous bond distance. The concept of bond distance to bond order relationship was first introduced by Tersoff[3] and, later, implemented within carbon environment by Brennan[4]. ReaxFF is based on this concept and formulates the potentials as functions of bond orders, while the bonds are allowed to dynamically form and dissociate. As such, in contrast to conventional classical inter-atomic potentials, the framework of ReaxFF allows chemical reactions to be properly described. In addition, the parameters of ReaxFF are fitted and optimized against an extensive database of quantum mechanics calculations and experimental data. All together, these features enable the simulations of large atomic systems, in complex chemical environments, with a computational cost comparable to that typically required by classical force fields.

The span of successful applications of ReaxFF includes a broad range of carbon-based systems[5–7], silicon and silicon oxide (crystal structures) systems[2,8], titania[9,10], aluminum and aluminum oxide systems[11], etc. ReaxFF has also been shown to accurately

describe the hydration of systems such as calcium–silicate–hydrates[12–14], and the mechanical properties of various materials[15–18]. In addition to crystalline solids, ReaxFF has been used to study the glassy silica–water interface[19] and organosilicate glasses[20]. In fact, the application of ReaxFF to silicate glasses is especially attractive, as their structure, which, in contrast to crystals, is not a priori known, remains poorly understood. However, non-crystalline structures are usually not taken into account during the development of potentials. As such, it remains unclear whether ReaxFF, primarily parameterized versus crystalline networks, can produce realistic glasses. Simulation of glasses is also particularly challenging, as simulated glasses are typically produced by quenching a system from its liquid state, thereby mimicking the experimental procedure used to form glasses. Indeed, such a methodology requires the used potential to offer a realistic description of the solid as well as the liquid and super-cooled liquid states. As such, there is a need to assess in details the ability of reactive potentials like ReaxFF to predict realistic structures for glassy materials.

The validation of ReaxFF potential is done by, first introducing the potential and its parameterization; second analyzing potential performance on fundamental systems such as silica and silicates with modifiers. The validity of further application of ReaxFF on the study of reactivity on fly ashes and cement is based on these preliminary assessments.

ReaxFF and its parameterization

ReaxFF partitions the total energy of an atomic system E_{system} into several energy components[21]:

$$E_{system} = E_{bond} + E_{over} + E_{under} + E_{lp} + E_{val} + E_{pen} + E_{torsion} + E_{conj} + E_{vdWaals} + E_{Coulomb}$$ **Equation 2**

where the components include, following the order above, bond energy, over-coordination energy, under-coordination energy, lone electron pairs energy, valence angle energy, penalty energy, torsion energy, conjugation energy, van der Waals energy and Coulomb potential energy. The prominent feature separating ReaxFF from conventional classical force fields is that the covalent interactions (e.g., bond energy, valence angle energy, torsion energy, etc.) are determined from a dynamic bond order, which is updated continuously from the instantaneous interatomic distances during a simulation[2]. In particular ReaxFF is able to formulate single, double and triple bonds ($BO^{\sigma}, BO^{\pi}, BO^{\pi\pi}$), each has separated dependence on the distance and different dissociation energies. The bond energy E_{bond} can be described by the following form:

$$E_{bond} = -D_e^{\sigma} BO_{ij}^{\sigma} \exp\left[p_{be,1}\left(1 - \left(BO_{ij}^{\sigma}\right)^{p_{be,2}}\right)\right] - D_e^{\pi} BO_{ij}^{\pi} - D_e^{\pi\pi} BO_{ij}^{\pi\pi}$$ **Equation 3**

where D and p are bond energy parameters and can be found in Ref. [2]. This allows ReaxFF to capture the dynamics of bond forming and breaking processes, which is required to simulate chemical reactions. The form of the function used for the bond order in ReaxFF also ensures that the covalent interactions disappear smoothly upon bond dissociation, after which only the non-bonded and Coulomb interactions play a role.

In addition, an implemented charge equilibration (QEq) method[22,23] allows the atom charges to be assigned dynamically. As such, the charge of an individual atom depends on its environment (e.g., its coordination number). This is a very attractive feature for glassy materials, as the coordination number of the atoms (like B or Al) can show some variability[24,25]. On the contrary, conventional classical force fields maintain constantly

the full or partial charges for each element. The QEq method also provides the convenient feature of having finite atom sizes, which shields Coulomb interactions at short distances and resolves the difficulties encountered by excluding the Coulomb interaction for dynamically bonded atoms. Similar short distance shielding is applied to van der Waals term as well[21].

ReaxFF also includes energy terms to account for various bond natures. The over-coordination is compensated by penalty energy (E_{over}) while E_{over} accounts for π electron between the bonded under-coordinated atoms. Furthermore, an additional energy penalty term E_{pen} is superimposed to ensure the stability of the system when two double bonds are sharing an atom in a valence angle. The heat of formation for non-conjugated closed shell molecules is reproduced through E_{conj} term. To determine all the parametric values used in ReaxFF, the parameters set is optimized against a large database containing data from quantum chemical calculations of both molecular and crystal systems, as well as from experiments. More details of these energy terms can be found in Ref. [2].

2.2 Introduction of Topological Constraint Theory (TCT)

A glass's response to mechanical stress is controlled by the topological of the disordered atomic network. Topological constraint theory can capture such features of atomic topology, while filtering out the details that do not significantly affect the macroscopic properties.

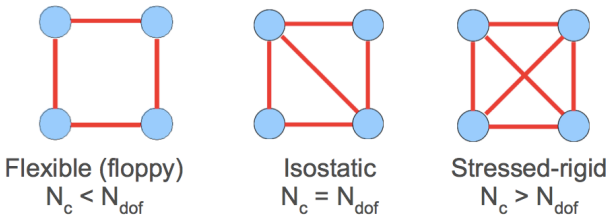

(a)

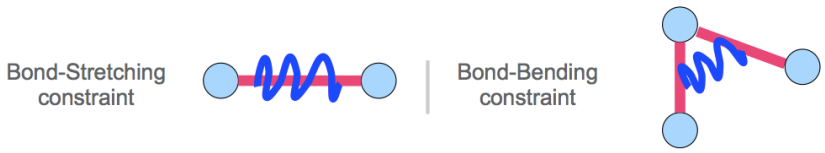

(b)

Figure 2: (a) The three rigidity states of a mechanical truss. (b) Schematic of the methodology used to compute the number of active BS and BB constraints through molecular dynamics simulations.

TCT, introduced by Philips[26], originally focused on the prediction of glass-forming domains of composition. Phillips predicted that the glass forming ability is optimal when the number of constraints acting between the atoms equals the number of atomic degrees of freedom. For network glasses, the constraints comprise: (1) the radial 2-body bond stretching (BS) interactions, maintaining the bond length fixed around their average values, and (2) the angular 3-body bond-bending (BB) interactions, which constrain the bond-angles. Staring from atoms having three translational degrees of freedom, each independent constraint removes one internal degree of freedom of the atomic network. As stated by Maxwell criterion of stability for mechanical trusses, atomic networks are flexible (under-constraint), stress-rigid (over-constraint), or isostatic (statically determinate), when the number of constraints per atom n_c is lower, higher or equal to three respectively. Here, the optimal glass forming ability is obtained for isostatic compositions.

This methodology will be applied to determine the rigidity of both crystalline and glassy materials. While there exists a vast range of compositions, and different atomic orderings for the same chemical composition, only a limited number of simulations are required to determine how many constraints are created by each atomic species (i.e. Si, O, Al, Na, Ca, K). Once such constraint data is available through molecular dynamics, number of constraints per atom n_c can be analytically calculated for any given glassy or crystalline composition.

Part III. Validation of the Interatomic Potentials

This Part is dedicated for validating the MD potentials that are used for further investigation of glass properties. ReaxFF in particular, is given extra attention due to its relative new existence.

Reactive potentials, like ReaxFF, are becoming increasingly popular and are expected to bridge the gap between *ab initio* and classical molecular dynamics simulations. Yet, their applicability to glassy materials remains poorly understood. Here, by simulating a silica glass and a sodium silicate glass with both ReaxFF and conventional classical potentials, we critically assess the ability of reactive potentials to offer accuracy equivalent or superior to that of classical potentials in describing the structure and properties of glassy silicates.

3.1 Silica Glass

Here, we focus on glassy silica, which serves as a structural basis for various multi-component silicate glasses of both industrial and geological interests[27]. By following a consistent procedure to form the glass, the outcome of the ReaxFF potential is compared to that of a conventional classical force field. ReaxFF is shown to offer realistic description of silica glass.

3.1.1 Glass Preparation

All simulations in this study are performed using the LAMMPS package[28]. The ReaxFF potential is implemented through the user-reaxc package. The outcome of ReaxFF are compared to that of classical molecular dynamics (MD), relying on the well-established

BKS potential[29], the potential which is probably the most commonly used for silica. Various potentials have been proposed before; each having their own advantages. Nonetheless, the BKS potential remains the most commonly applied potential, thanks to its simple formulation. Although we keep in mind that some superior force fields are available, such as polarizable interatomic force fields[30], they usually have more complex forms and, therefore, come with higher computational cost. On the other hand, despite its simplicity, the BKS potential has been shown to produce a realistic bulk structure for silica[31,32]. Here, we use a modified version of the original BKS potential, with a short-range cutoff 5.5 Å and long range Coulomb interaction cutoff 10.0 Å[33].

Three methods are tested in this study. (1) A glass is formed via quenching a liquid from 4000K to 300K fully using ReaxFF (ReaxFF method). (2) A glass is formed via quenching a liquid from 4000K to 300K fully using the BKS potential (classical method). (3) A glass is first formed via quenching a liquid from 4000K to 300K using the BKS potential, then equilibrated at 300K with ReaxFF (hybrid method). Here, the hybrid method is tested as a potential option to avoid the higher computational cost of ReaxFF with respect to usual classical MD during the cooling phase.

More specifically, SiO_2 units (4536 atoms) are first randomly distributed inside a cubic box, by ensuring no unfavorable overlap between the atoms. Then, we assure the loss of the memory of the initial configuration by melting the system at 4000K for 100ps. The silica glasses are then prepared by linearly reducing the temperature of the system, from 4000K to 300K. The formed glass is subsequently equilibrated at 300K for an

additional 1ns, although no additional relaxation is observed at this point. The NPT ensemble, ensuring a zero pressure, is applied throughout the process. In the case of the hybrid method, a glass is first produced with the BKS potential by cooling the liquid from 4000K to 300K, before being subsequently relaxed with the ReaxFF potential at 300K for 1ns. This length of time was found to be sufficient to ensure the equilibration of both the energy and the volume of the system. Due to the high bonding energy of SiO_2, we do not observe any changes in the connectivity of the network, that is, no bond is broken or created during the relaxation process at 300K. Note that a consistent cooling rate of 1 K/ps is used for all the three methods. Previous studies have shown that such a cooling rate is sufficient to obtain a realistic glass structure[33–35], even though it is considerably higher than those used in experiments. Note that cooling rates as high as 5-to-10 K/ps are commonly used in MD simulations, due to the computational cost of the technique. The effect of the cooling rate has recently been carefully evaluated[36] and, although the density and thermal expansion appear to be affected, most of the structural features of the glass remain unchanged.

3.1.2 Results

Medium-range order

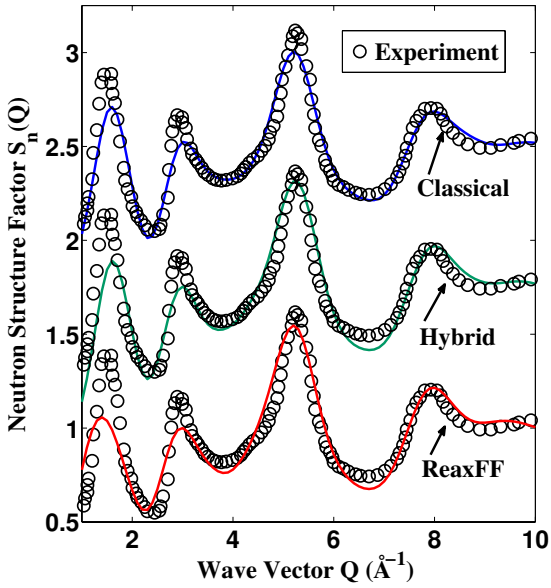

Figure 3: Computed neutron structure factors of the simulated glasses, as prepared with the ReaxFF, hybrid and classical methods (lines). The results are compared each with the same data from diffraction experiments[37].

To assess the simulated structures of silica glass, we first compute the neutron structure factor $S_N(Q)$ by calculating the Fourier-transform of the partial pair distribution functions (PDF) $g_{ij}(r)$. The spurious ripples at low Q caused by the finite cutoff used during the Fourier-transform are suppressed by applying a Lorch-type window function[38]. The obtained neutron structure factors are shown in Figure 3, and compared with results from diffraction experiments[39].

As shown in Figure 3, we observe a very good overall agreement in the high Q range for all the three methods, which suggests a well-reproduced short-range structure. In low Q range, however, some discrepancies are observed around 1.5 $Å^{-1}$ at the first

sharp diffraction peak (FSDP), which suggests that these three methods predict slightly different medium-range orders. Specifically, the BKS potential presents a shift of the FSDP to larger *Q* values with respect to what is obtained experimentally, whereas the ReaxFF method predicts a slightly smaller value. We also note that the structure obtained with the hybrid method is similar to that of ReaxFF at large *Q*, whereas in the low *Q* region, the FSDP remains reminiscent of that of predicted by the BKS potential.

Table I. Computed densities of the simulated glasses, as prepared with the three methods. The results are compared with the experimental density.

	Classical	Hybrid	ReaxFF	Experiment[a]
Density (g/cm^3)	2.22	2.34	2.18	2.20

[a] Experimental density is from Ref. [40].

In fact, these discrepancies are manifested in the density of the formed glasses, which are tabulated in Table I. Computed densities of the simulated glasses, as prepared with the three methods. The results are compared with the experimental density. A strong correlation between the position of the FSDP (Q_{FSDP}) and the density has been noted in previous studies, i.e., larger Q_{FSDP} implies a smaller distance of structural repetition and, hence, higher density, and vice versa[41]. Such a trend is in accordance with what is observed in the present study. Here, the density predicted by the ReaxFF method is slightly lower than the experimental value, while the classical method gives a slightly higher prediction. The levels of deviation of these two methods are on the same level, at about 0.02 g/cm^3. We note that the hybrid method, on the other hand, produces a larger deviation of 0.14 g/cm^3. Although the level of agreement is similar for the ReaxFF and BKS potentials, it is worthwhile to point out that the BKS potential used in the study has

been specifically parameterized to reproduce the density of glassy silica and, for instance, would not predict a correct density for quartz with the same cutoff. On the contrary, ReaxFF is expected to be transferable to a large number of compounds, in various chemical environments. Hence the fact that the ReaxFF method yields the same level of agreement as compared to BKS is encouraging.

Short-range order

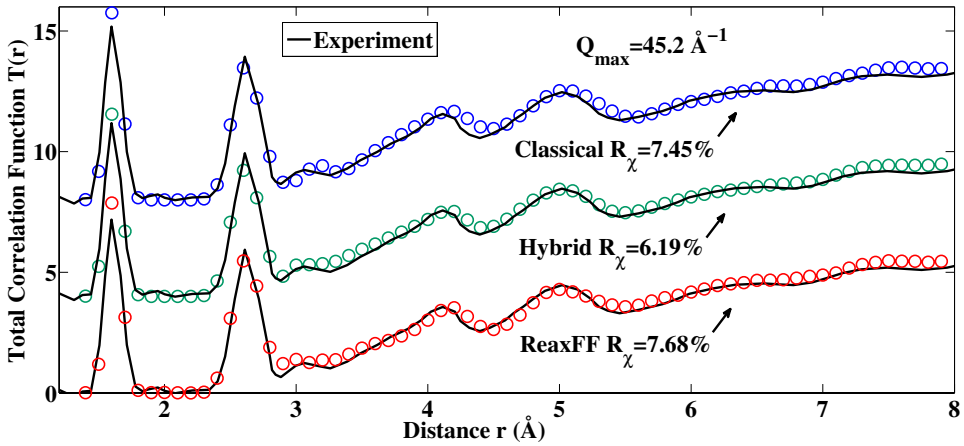

Figure 4: Computed total correlation functions of the simulated silica glasses, as obtained by the three methods (circles). The results are compared with the same experimental data (solid lines), obtained by neutron diffraction[37]. For each method, the calculated R_χ factors are shown.

Although it contains the same level of information as the structure factor, the total correlation function (TCF) emphasizes the short-range order. As such, both of them should be compared to experiments to assess the quality of a potential. The TCFs, as calculated for the glasses obtained by the three considered methods, are shown in Figure 4. It is worth noting that the diffraction instruments used in experiments have a finite scattering wave vector (Q_{max}). Hence, for meaningful comparisons, we broaden the calculated TCFs using the method described by Wright[42].

To assess the level of agreement between the computed and experimental TCFs, we adopt Wright's method and calculate the R_χ factor between 1Å and 8Å, which is given by the following equation:

$$\boldsymbol{R_\chi} = \left[\frac{\sum_{i=1}^{n}(g(r)-g_{\mathbf{ref}}(r))^2}{\sum_{i=1}^{n}(g_{\mathbf{ref}}(r))^2}\right] \qquad \textbf{Equation 4}$$

where $g_{\mathrm{ref}}(r)$ is the experimental TCF and *n* is the total number of points for the TCF. Considering that a R_χ factor of less than 10% is typically considered to represent a good agreement, we note that all the three methods provide a realistic overall structure, with R_χ factors around 6% to 7%. However, when averaged on all pairs of atoms, TCFs and structure factors usually reveal to be largely unaffected by the details of the potentials[25]. A more detailed analysis of the environment of each atom is therefore required.

Table II: Computed average Si–O bond lengths for three methods, compared with available experimental values.

	Classical	Hybrid	ReaxFF	Experiment
Average Si–O Bond Length (Å)	1.616	1.613	1.615	1.608[a]/1.610[b]

[a] Experimental Si–O bond length is from Ref. [37].
[b] Experimental Si–O bond length is from Ref. [43].

In order to gain more insight into the short-range structure, partial pair distribution functions (PDFs) are calculated for Si–O, O–O and Si–Si pairs. The first peak of the partial PDFs, as shown in Figure 3–5, corresponds to the first coordination shell of each element, and allows us to calculate the average inter-atomic bond distances. We note that, for both the Si–O and O–O PDFs (Figure 5 and Figure 6) no significant differences

are observed among the three methods. All the three methods also have an average bond length that is in excellent level of agreement with experiments (see Table II).

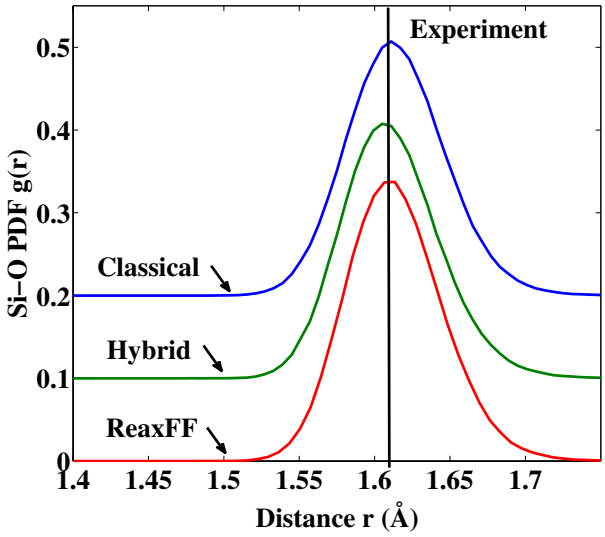

Figure 5: Computed Si–O pair distribution functions, as obtained by the three methods. Available experimental values of the average Si–O bond length are represented by solid vertical lines[37], [43]. Note that, here, the spread of the experimental values is too small to be visible.

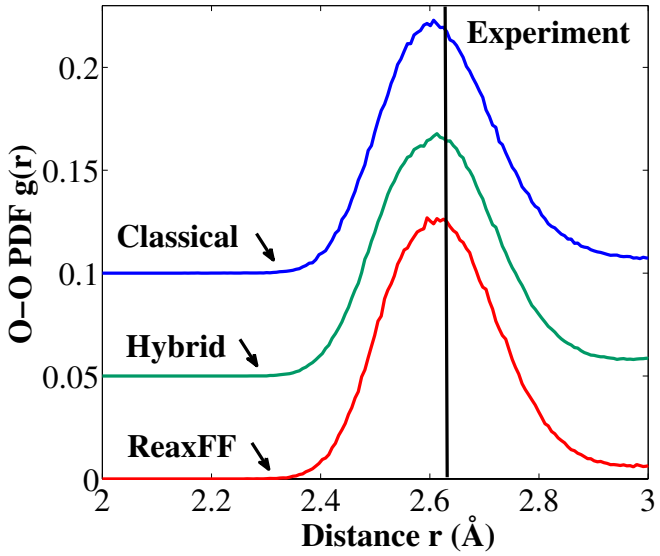

Figure 6: Computed O–O pair distribution functions, as obtained by the three methods. The experimental value of the average O–O bond length is represented by a solid vertical line[37].

The coordination number of each species is calculated by directly enumerating the number of neighbors of each atom, with a distance cutoff defined by the first minima after the main peak of the PDFs. The results are shown in Table II. Overall, we find a good agreement with experimental observations, as all methods predict a realistic tetrahedral environment for Si atoms, with a coordination number of around 4[40].

Table III: Computed coordination numbers of Si atoms, compared with the experimental value.

	Classical	Hybrid	ReaxFF	Experiment [a]
Si Coordination Number	4.00	3.99	3.99	3.95

[a] Experimental coordination number is from Ref. [40].

On the contrary, a noticeable difference among the three methods is observed for the Si–Si PDF. As shown in Figure 7, the three methods predict significantly different shapes and average values for the first peak of the PDF. First, in agreement with previous studies[32], the BKS potential (classical method) predict a largely symmetric distribution, centered on 3.11 Å. In contrast, both the ReaxFF and the hybrid methods show an asymmetric distribution, centered at lower distances. We note, however, that the hybrid method features a more pronounced shoulder around 3.13 Å, reminiscent of the distribution obtained by the classical method. Since the three methods predict a similar Si–O bond length, the present difference observed in the average Si–Si distance

obviously arises from differences in the Si–O–Si (inter-tetrahedral) bond angle. It is therefore useful to take a closer look at the Si–O–Si angular distribution.

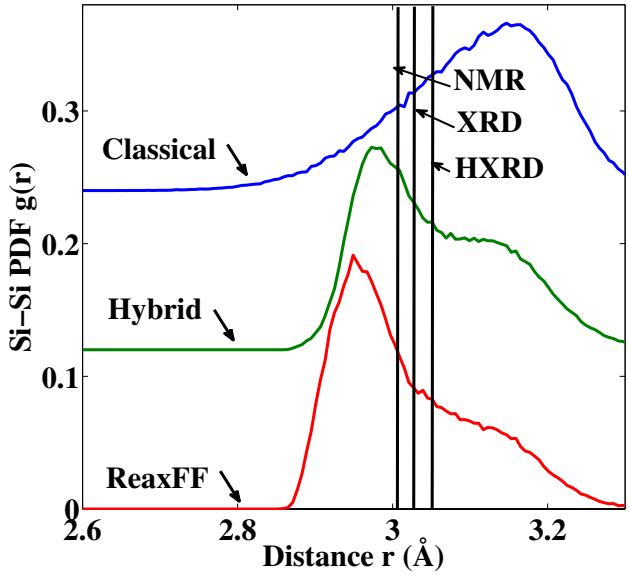

Figure 7: Computed Si–Si pair distribution functions, as obtained with the three methods. The vertical lines indicates available experimental data of the average Si–Si bond distance, calculated from the experimental Si–O–Si average angles[44–46] and Si–O distances[37].

Bond angle distributions

As expected, the Si–O–Si bond angle distributions (BADs), as shown in Figure 6, also show different shapes and averages values. In agreement with previous studies[32], the BKS classical potential predicts a symmetrical distribution, centered on 152°. In contrast, the ReaxFF potential predicts an asymmetrical distribution, with an average value shifted to lower angle. The hybrid method, once again, retains some features from both the classical and ReaxFF methods, which manifests by an asymmetric distribution featuring a pronounced shoulder reminiscent from the peak predicted by the classical method. Overall, based on the average value of the angle, we observe a reasonable agreement with the available experimental data for ReaxFF. We also note that the

distribution produced by the classical method has a full width at half maximum (FWHM) similar to that obtained from standard X-ray diffraction (XRD) (see Table IV), but significantly larger than that obtained by nuclear magnetic resonance (NMR) spectroscopy and high energy XRD (HXRD). However, since the broad FWHM obtained from standard XRD is likely to be largely affected by the instrument (e.g., X-ray source) being used, the Si–O–Si BAD predicted by the BKS potential appears unrealistically wide. On the other hand, the ReaxFF potential predicts a more realistic narrower distribution, which can potentially offer a better description of the SiO_2 network geometry. We also note that experiments suggest the existence of an asymmetrical distribution[47], in order to compensate the Si–Si distance constraint[48]. However, it is important to recognize that experimental data with higher resolution would be helpful for any further evaluation.

The Si–O–Si BAD obtained from *ab initio* simulation[49] is also included for comparison in Figure. 8. We note that the obtained average value of the BAD (141°) shows a better agreement with the one predicted by ReaxFF, rather than with the one predicted by BKS. However, the distribution obtained by *ab initio* simulations shows a lower degree of asymmetry as compared to that predicted by ReaxFF. It should be kept in mind that *ab initio* simulation come their own limitations, which make it challenging to use their outcome as absolute references. In the present case, the very limited size of the system (72 atoms) and the extremely high cooling rate (on the order of 100 K/ps) used in the *ab initio* simulation could greatly affect the shape of the Si–O–Si BAD. In fact, a recent study focusing on the the role of the cooling rate[36] indeed showed that the Si–O–Si BAD

is the structural feature that is the most sensitive to the used cooling rate. As such, no solid conclusions can be drawn here by comparing the outcome of ReaxFF and BKS with that of *ab initio* simulations.

Table IV: Computed mean bond angle and full width at half-maximum (FWHM) of the Si–O–Si bond angle distributions obtained with the three methods compared with experimental values from NMR, HXRD and XRD are listed for comparison.

	Classical	Hybrid	ReaxFF	NMR[a]	HXRD[b]	XRD[c]
Mean Bond Angle	152°	145°	140°	142°	147°	144°
FWHM	35°	15°	14°	26°	17°	38°

[a] NMR experiment values are from Ref. [45].
[b] HXRD experiment values are from Ref. [44].
[c] XRD experiment values are from Ref. [46].

The O–Si–O (intra-tetrahedral) BAD is also computed and shown in Figure. 9. As expected, all the three methods produce a similar average peak value, at about 109°, characteristic of the tetrahedral environment of the Si atoms.

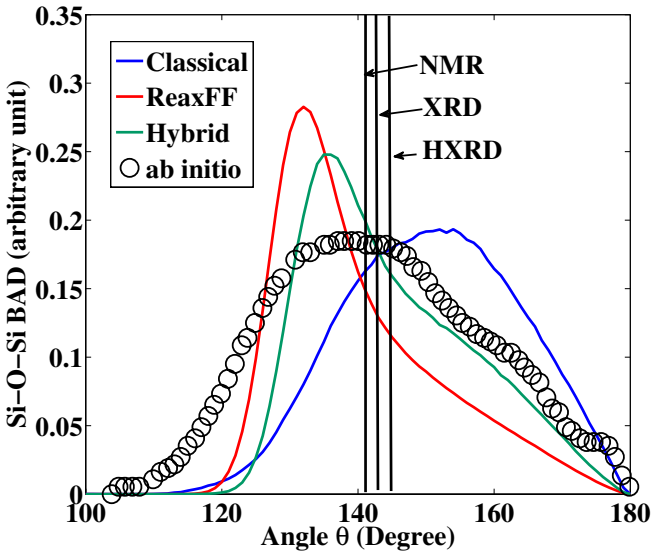

Figure. 8. Computed Si–O–Si bond angle distributions obtained for the three methods and ab initio[49]. In each case, the average value of the distribution is indicated and compared to experimental values obtained from NMR[45], HXRD[44] and XRD[46], represented by solid vertical lines.

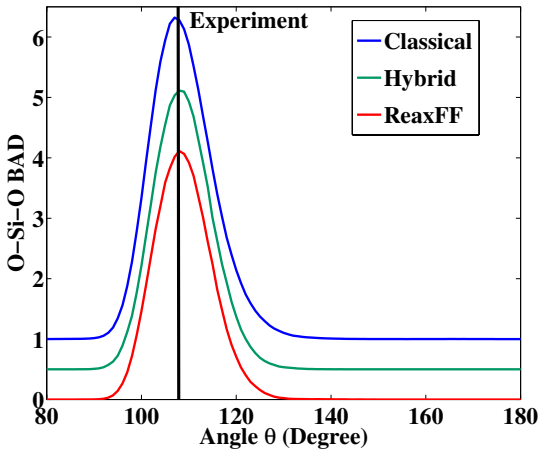

Figure. 9. Computed O–Si–O B bond angle distributions obtained for the three methods, compared with the experimental value of the average angle, represented by a solid vertical line[37].

Elasticity

Next, the mechanical properties of the obtained glasses are examined by calculating the Young's and shear moduli. Arguably, if the structure of a glass as captured, e.g., by the PDF is rather easy to reproduce, even for poorly parameterized potentials, the elastic properties, which depend on the curvature of the potential, are more challenging to predict. Indeed, the elastic moduli computed for the glasses obtained by the three methods (shown in TABLE V) exhibit substantial variations. First, we note that the BKS potential over-predicts by more than 20% the shear modulus and by more than 30% the Young's modulus. These values are in agreement with previous studies and constitute a known limitation of the potential[50]. We note that the ReaxFF potential offers an excellent agreement with experiments[51]. On the contrary, the hybrid method leads to values fairly consistent with those predicted by the BKS values and, thereby, is in poor agreement with experiments. Nevertheless, the ability of ReaxFF to predict elastic properties in excellent agreement with experiments is all the more remarkable since ReaxFF has not been parameterized with respect to glassy silica.

TABLE V. Computed shear and Young's moduli of the glasses obtained by the three methods, compared with experimental data. Error bars are given in parenthesis.

	Classical	Hybrid	ReaxFF	Experiment [a]
Shear modulus(GPa)	40.1 (1.5)	42.0 (0.4)	32.2 (0.8)	31.3
Young's modulus (GPa)	101.5 (2.9)	104.6 (1.1)	80.4 (1.9)	72.9

[a] Experimental moduli are from Ref. [51].

Self-diffusion

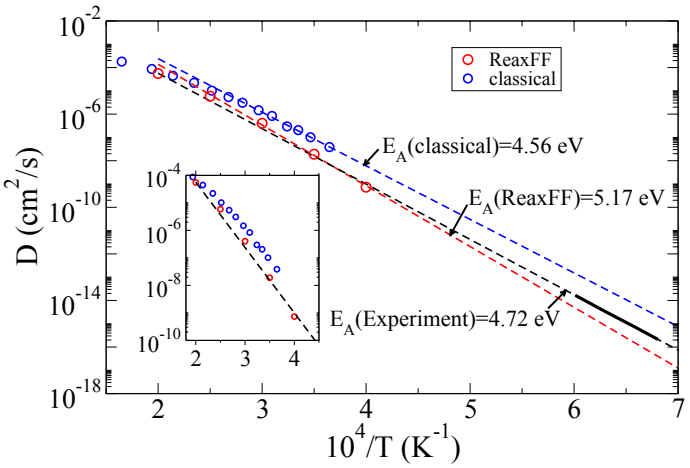

Figure 10: Computed self-diffusion constants of the O atoms in the supercooled liquid state, using the BKS (blue circles) and ReaxFF (red circles) potentials. The values are compared with available experimental data (solid black line)[52]. For comparison, the simulated and experimental values are extrapolated (dashed lines) to higher and lower temperature, by assuming an Arrhenius-like behavior. The inset contains the same data, zoomed on the high temperature range.

Finally, we evaluate ReaxFF's ability to simulate the dynamics of the supercooled glass-forming liquid, that is, at temperature larger than the glass transition temperature (T_g). We calculated the mean-square displacement (MSD) versus time of the O atoms and checked that a diffusive regime is obtained, which manifests by a slope of one in log-log scale. The self-diffusion constants D of the O atoms in the silica glass-forming liquid were then evaluated by fitting the MSDs with the Einstein equation in the diffusive regime. Note that, since the simulations are performed with equilibrated liquids above T_g, the distinction between the full ReaxFF and hybrid methods is no longer relevant, and the results reflect solely the properties of the respective force fields.

Figure 8 shows the self-diffusion constants with respect to the inverse of the temperature *T*, for the ReaxFF and classical (BKS in this case) methods. An Arrhenius type behavior, which manifest by a linear evolution in logarithm scale, can be clearly identified for both methods. This allows us to compare our results with the experimental data obtained at lower temperature by directly extrapolating the calculated values[52]. It is however important to point out that the simulated diffusion constants, especially those simulated with the BKS potential, eventually begin to show a non-linear behavior at higher temperatures. We therefore exclude these non-linear portions from the extrapolation.

As shown in Figure 10, a substantial difference in the magnitude of the diffusion constants is observed between the ReaxFF and BKS potentials. We observe that the diffusion constants predicted by the BKS potential are systematically about one order of magnitude higher than the extrapolated experimental data (see the insert of Figure 8). In contrast, ReaxFF offers a significantly better agreement in term of the magnitude. At the same time, the activation energy, as calculated from the slope of the lines shown in Figure 8, is well reproduced by both ReaxFF and BKS. The ReaxFF potential predicts an activation energy of 5.17 eV, as compared to 4.52 eV for BKS, with the experimental result being 4.72 eV.

3.1.3 Discussion

As mentioned before, most classical inter-atomic potentials typically succeed in predicting a reasonable structure for glasses. Indeed, any rough parameterization would

lead to the correct bond distances and coordination numbers. However, ReaxFF appears to offer significant enhancements for properties that are more sensitive to the details of the potential, like the elastic moduli or the diffusion constants. Clearly, further studies would be needed to better understand if these improvements arise from the specific features of ReaxFF (dependence of the potential on the local environment, ability to break and form bonds, and use of non-constant charges), or if a better parameterized conventional classical potential would offer the same level of performance. However, it can reasonably be assumed that the ability to break and form bonds plays a critical role to produce a realistic mechanism for the diffusion. As the atomic diffusion in silicate supercooled liquids is believed to occur through a hoping mechanism[53,54], involving the creation of over- or under-coordinated intermediate species, the dependence of the potential to the local environment of the atoms is also likely to explain the better prediction of the self-diffusion constants magnitude in silica by ReaxFF. This is also encouraging in that an improved description of the dynamics would ensure a more realistic cooling process and, as a result, a more reasonable structure in the final glassy state.

Although similar hybrid methods have been adopted before (e.g., in DFT simulation of glasses[55,56]), we found that, in the case of silica, it produces a structure with mixed features arising both from the classical and ReaxFF potentials, rendering it less desirable. We therefore do not recommend using the hybrid method for silica. Indeed, the hybrid method appears to preserve, to some degree, the medium-range order obtained with the classical method (as evidenced by the position of the FSDP and Si–Si PDF/Si–O–Si BAD shoulder), while adopting the short-range order predicted by the

ReaxFF potential. This is not surprising since, although local relaxation events (like some variations of the average angle) are possible after switching from the BKS to ReaxFF potential, larger range relaxation is not likely to occur. In fact, changing the medium range order of the glass, e.g., by changing the ring statistics, would require breaking and reforming bonds, which would be very unfavorable at room temperature and is, indeed, not observed in the present simulations.

At the same time, it is worth noting that, for glasses featuring a less rigid network (e.g., alkali or alkaline earth silicates), the hybrid method may perform better, as the glass structure will allow a higher degree of relaxation. This will be tested in future studies. Indeed, as using the ReaxFF potential through the entire cooling process involves a higher computational cost, directly relaxing with ReaxFF some glassy structures produced by cheaper classical MD would be an attractive option.

As such, it is clear that the hybrid method offers a glass structure, for which the short- and medium-range orders are characteristic of the predictions by the ReaxFF and BKS potentials, respectively. Overall, this method appears to lead to an acceptable structure, which manifests by a good agreement of the TCF with neutron diffraction data. However, based on the present results, such an approach can be problematic for the properties that do not only depend on the short-range order. As a matter of fact, as indeed observed here, the Young's and shear moduli predicted by the hybrid method show a poor agreement with experiments. Once again, this is not surprising as, although the elastic moduli strongly depend on the stiffness of the individual bonds and

angles, it is also sensitive to the medium-range topology of the glassy network. Clearly, merely restoring the structure and interactions at the short-range, without a proper medium-range order, is not sufficient to predict realistic material properties.

This study also highlights the fact that, to assess the quality of an inter-atomic potential, it is required to look beyond the usual structure characterizations (PDF and structure factor) and to perform an in-depth characterization of the environment of each element, as well as to compute more advanced properties like the elasticity.

3.2 Sodium Silicate Glass

Here, an archetypal modified silicate glass, sodium silicate glass, is simulated using the ReaxFF potential. The predicted structure is critically evaluated and compared to that obtained by a classical potential and experimental data. Our results indicate that ReaxFF offers an improved description of the atomic structure, both at the short- and medium- range.

3.2.1 Glass Preparation

To evaluate the ability of ReaxFF to simulate modified silicate glasses, we consider a sodium silicate glass with a composition of $(Na_2O)_{30}(SiO_2)_{70}$. The simulations are performed with the LAMMPS package[28]. The outcome of ReaxFF is compared to that obtained from conventional classical MD, relying on the well-established Teter potential[57]. Note that, despite the simplicity of its formulation, the Teter potential has been shown to reproduce realistic structural, elastic, dynamical, vibrational properties for sodium silicate glasses[33–39].

The silicate system, made of 3000 atoms, is first formed by randomly distributing atoms inside a cubic box, while ensuring no unrealistic overlapping. The system is then melted at 4000 K for 100 ps in order to ensure the loss of the memory of the initial configuration. The silicate glass is then formed by linearly reducing the temperature from 4000 K to 300 K with a cooling rate of 1 K/ps. Even though this cooling rate is noticeably higher than typically used experimental ones, it is, based on previous studies[33–35], low enough to produce realistic glasses. The effect of the cooling rate has recently been thoroughly evaluated[36] and, although the density and thermal expansion appear to be slightly affected, most of the structural features of the glass remain unchanged. After cooling, the system is further equilibrated at 300 K for another 1 ns. The NPT ensemble, which ensures a zero pressure of the system, is applied for the entire process. Note that, for computational efficiency, the Teter potential is used through the glass formation. The structure of the obtained glass, as obtained with classical MD, is then fully characterized. In addition, the formed glass is further relaxed with the ReaxFF potential for 1 ns in the NPT ensemble at zero pressure, before structural characterization. Note that this duration of relaxation is found to be sufficient to ensure the convergence of both volume and energy. Table VIII shows the obtained final densities, which are both in good agreement with the experimental data[51].

Table VIII: Densities of the simulated glasses prepared with the classical and ReaxFF potentials, compared with experimental data.

	Classical	ReaxFF	Experiment[a]
Density (g/cm^3)	2.406	2.371	2.470

[a] The experimental density is taken from Ref. [51].

3.2.2 Results

Neutron structure factor

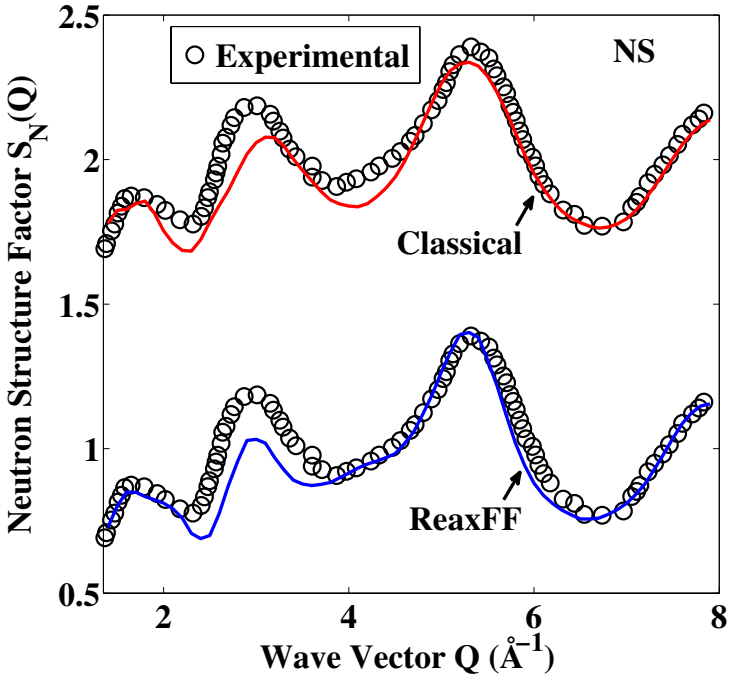

Figure 11: Calculated neutron structure factors of the simulated sodium silicate glasses, as predicted by the ReaxFF and classical potentials (solid lines). Each result is compared with experimental data (circles)[61].

In order to assess the structure of the simulated sodium silicate glass, the neutron structure factor $S_N(Q)$ is obtained by calculating the Fourier transform to the partial pair distribution functions (PDF) $g_{ij}(r)$. The obtained neutron structure factors are shown in Figure 11, where a Lorch-type window function[38] is applied to suppress the ripples at low Q caused by the finite cutoff during the Fourier-transform. We note that the classical MD and ReaxFF offer significantly different predictions for the first sharp diffraction peak

(FSDP), around 3 $Å^{-1}$. As seen in Figure 11, the position of the FSDP predicted by classical MD appears shifted to higher wave vector with respect to neutron diffraction data[61]. In contrast, the peak position predicted by ReaxFF is in excellent agreement with experimental data[61]. Furthermore, ReaxFF predicts a left-skewed peak symmetry, which also matches the experimental data.

Radial distribution function

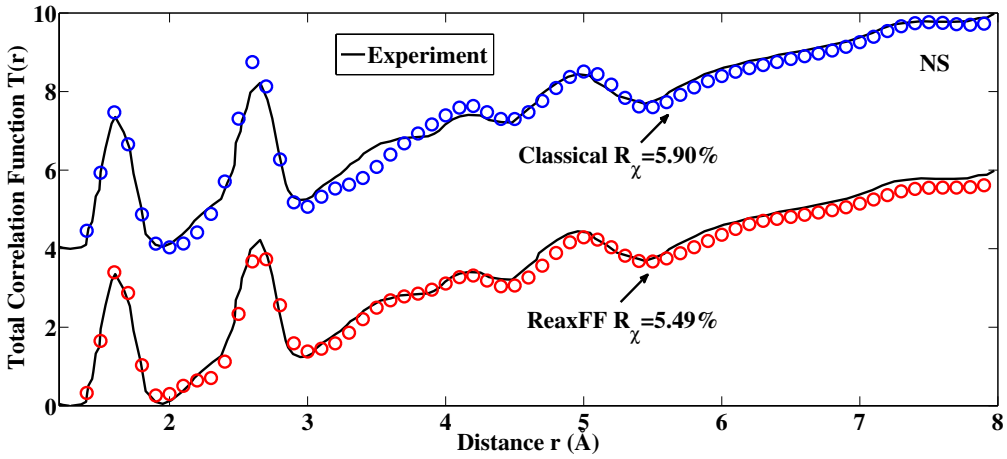

Figure 12 Calculated total correlation function for the sodium silicate glass, as predicted by the ReaxFF and classical potential (circles). The computed results are compared with neutron diffraction data (soid lines). R_χ factors are shown for each method (see text for details).

The total correlation function (TCF), although containing the same amount of information as the structure factor, emphasizes the short-range order. The TCFs calculated by both methods are shown in Figure 12. Note that, since the diffraction instruments used in experiments have a finite scattering wave vector (Q_{max}), the calculated TCFs are broadened following method described by Wright for meaningful comparisons[42].

The level of agreement between that computed and experimental TCFs can be quantified by the R_χ factor proposed by Wright[42], which is given by:

$$\boldsymbol{R_\chi} = \left[\frac{\sum_{i=1}^{n}(g(r)-g_{\mathbf{ref}}(r))^2}{\sum_{i=1}^{n}(g_{\mathbf{ref}}(r))^2}\right] \qquad \textbf{Equation 5}$$

where *n* is the number of points for the TCF and $g_{\mathrm{ref}}(r)$ is the experimental TCF. The R_χ factors obtained herein, calculated between 1 Å and 8 Å, are shown in Figure 12. Since a R_χ factor lower than 10% is typically considered to represent a good agreement with experiment, we note that both methods provide a realistic overall atomic structure, both R_χ factors being around 5%. However, since the TCFs and structure factors are averaged on all pairs of atoms and are usually weakly affected by the details of the potential[25], a more detailed study the local environment of each element is needed to evaluate the relative performance of the potentials.

The glasses are further analyzed by computing the partial pair distribution functions (PDFs) for the Si–O, O–O, and Si–Si pairs, which characterize the short-range order of the silicate network. As shown in Figure 13, the Si–O bond length predicted by the ReaxFF potential (1.620 Å) is higher than the one predicted by the Teter potential (1.609 Å) and is in good agreement with the experimental value (1.631 ± 0.06 Å). ReaxFF also predicts an O–O bond length (2.641 Å) that is in good agreement with the experimental value (2.660 ± 0.11 Å). Finally, the Si–Si bond length predicted by ReaxFF (3.012 Å) shows the same level of agreement as that predicted by the Teter potential (3.172 Å), the obtained values being lower and higher than the experimental one (3.093 ± 0.04 Å), respectively. Since ReaxFF describes accurately the Si–O bond, this discrepancy regarding the Si–Si bond is likely to arise from the inter-tetrahedral angle

(Si–O–Si), which is presented in detail in the next section. The bond lengths of prescribed species are shown in Table IX.

Table IX Si–O, O–O, and Si–Si bond lengths in sodium silicate predicted by ReaxFF and classical MD, and compared with available experimental values. The standard deviations for the experimental values are in parenthesis.

NS Bond Length	ReaxFF	Classical (Teter)	Experiment
Si–O (Å)	1.620	1.609	1.631[a] (0.06[a])
O–O (Å)	2.641	2.622	2.660[a] (0.11[a])
Si–Si (Å)	3.012	3.172	3.093[b] (0.04[b])

[a] The experimental Si–O and O–O bond lengths are taken from Ref. [62].

[b] The experimental Si–Si bond length is obtained from the Si–O–Si bond angle in Ref. [63] and Si–O bond length in Ref. [62] using trigonometric relationship.

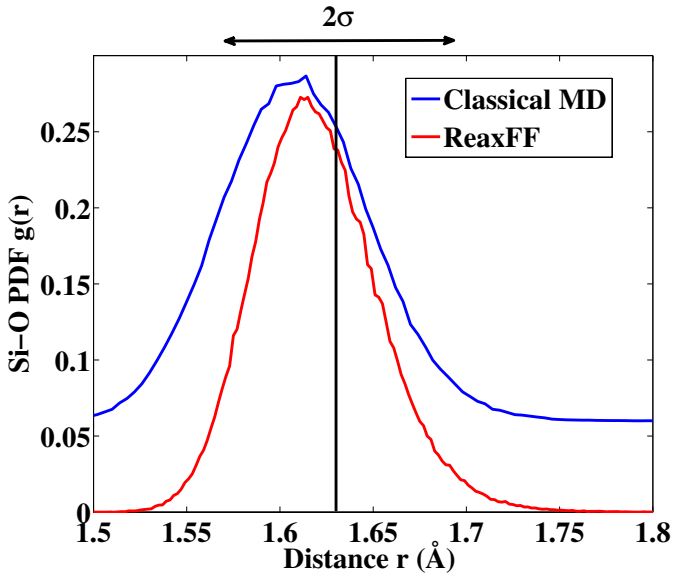

Figure 13 Si–O pair distribution functions predicted by both methods. The experimental Si–O bond length[62] is shown by the vertical solid line, with error bounds[62] shown by double arrows.

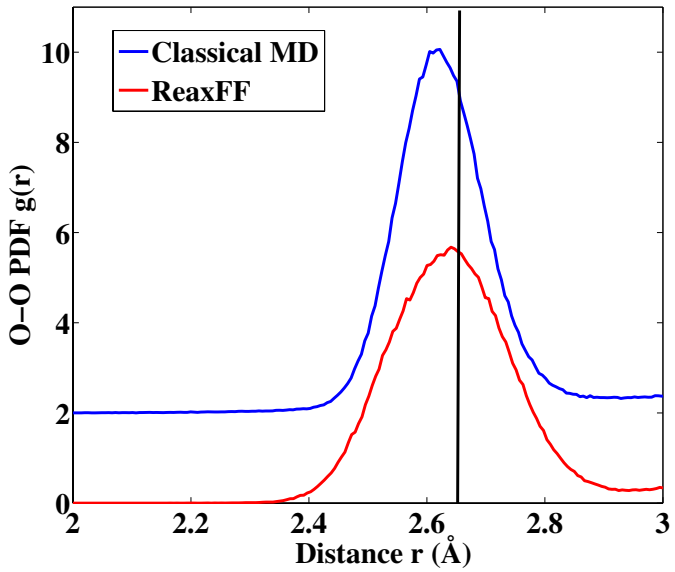

Figure 14 O–O pair distribution functions predicted by both methods. The experimental values of the average O–O bond length[62] is represented by the vertical solid line.

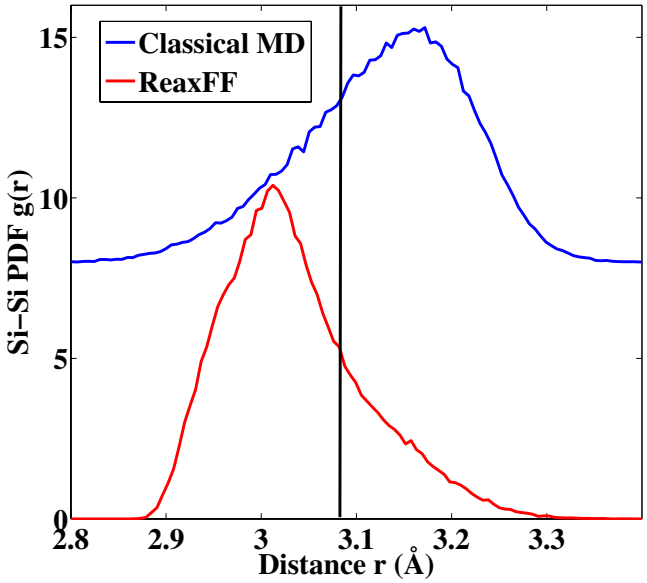

Figure 15 Si–Si pair distribution functions predicted by both methods. The experimental Si–Si bond length[62], calculated from the Si–O–Si bond angle[63] and Si–O bond length[62], is represented by the vertical solid line.

Bond angle distribution functions

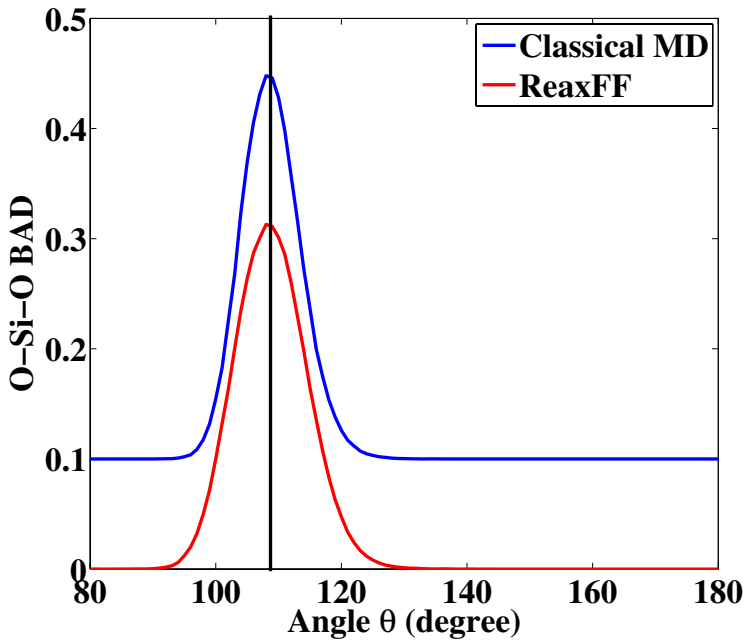

Figure 16 Computed O–Si–O bond angle distributions obtained by both methods. Theoretical O–Si–O bond angle distributions value in tetrahedral environment is represented by vertical solid line.

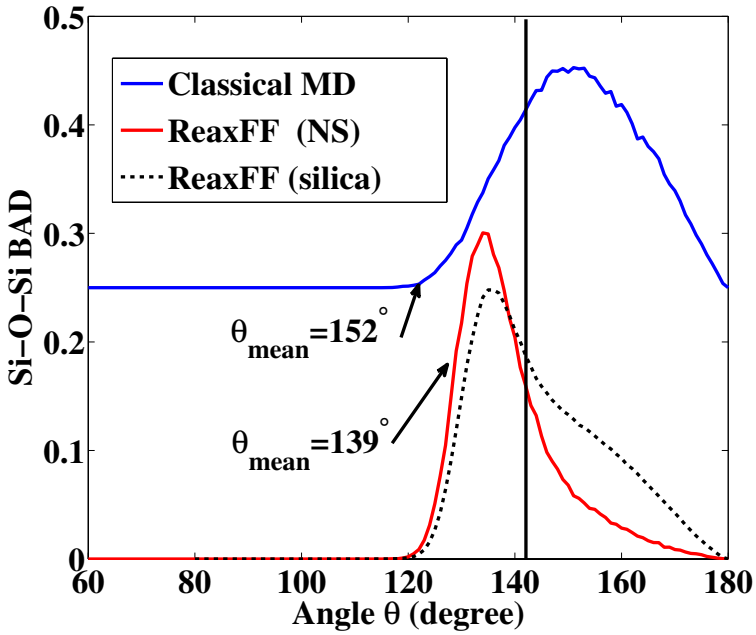

Figure 17 Computed Si–O–Si bond angle distributions obtained by both methods (in solid lines). The experimental average Si–O–Si bond angle[63] is represented by vertical solid line. In the case of ReaxFF, the bond angle distribution of sodium silicate is compared with that obtained for pure silica[64], using the same ReaxFF potential (dashed line). The mean bond angles of sodium silicate (both methods) are shown in text with arrow pointed to the curve.

We now focus on the angular environment of each element. The O–Si–O (intra-tetrahedral) and Si–O–Si (inter-tetrahedral) bond angle distributions (BADs), as predicted by the ReaxFF and classical potentials, are calculated and compared. As shown in Figure 16, both classical MD and ReaxFF predict a O–Si–O BAD centered around 109°, in agreement with the tetrahedral environment of the Si atoms.

As previously discussed, the discrepancy between the Si–Si PDFs predicted by the ReaxFF and Teter potentials directly results from different inter-tetrahedral BADs. As shown in Figure 17, classical MD predicts an average angle value of 152° and a full width at half maximum (FWHM) of 33°. In contrast, ReaxFF offers an average angle of

139° with a smaller FWHM of 15° (see Table X). For comparison, the experimental values for average bond angle and FWHM are included in Table XTable X. Overall, we observe that ReaxFF offers an improved level of agreement with the experimental data, both for the average Si–O–Si angle and its FWHM. On a different note, we note that, as opposed to the Teter potential, ReaxFF predicts an asymmetric Si–O–Si BAD, which is likely to arise from steric Si–Si repulsions. Such asymmetry is supported by experiements[48].

Table X Calculated average bond angle and full width at half maximum (FWHM) of the main peak from both methods, for inter-tetrahedral BAD in sodium silicate glass.

	ReaxFF	Classical	Experimental
Average bond angle (°)	139	152	143[a]
FWHM (°)	15	33	21[a]

[a] The experimental values are obtained from a ^{17}O NMR study of a potassium silicate glass for comparison, see Ref. [63].

BO/NBO and Q_n distribution

Theoretical, the addition of sodium atoms affects the silicate network in the way that, each sodium atom creates one NBO. This mechanism is confirmed by XPS experiment[65]. Here (see), we provide the percentage of BO and NBO compared with theoretically calculated percentage, for the glass with 30% Na_2O. In addition, to observe the effect from changing sodium content, a sodium silicate glass with 20% Na_2O formed by same method, is used herein.

Furthermore, a comparison of the Q_n of the glasses with 30% and 20% Na_2O content, with Teter potential and NMR experimental results[66] has been made (see Table XI).

Table XI Calculated percentages of BO and NBO compared to theoretical values (in parenthesis), for sodium silicate glasses with 30% and 20% Na_2O content.

	30% Na_2O	20% Na_2O
BO (%)	77.8 (77.8)	64.7 (64.7)
NBO (%)	22.2 (22.2)	35.3 (35.3)

Table XII Calculated Q_n distribution for sodium silicate glasses with 30% and 20% Na_2O content, compared to NMR results included in parenthesis.

mol% Na_2O	Q_4 (%)	Q_3 (%)	Q_2 (%)
Hybrid 20	56 (50[a])	38 (48 [a])	5 (3[a])
30	36 (17[a])	45 (71[a])	18 (6[a])
Teter 20	57 (50[a])	36 (48[a])	7 (3[a])
30	34 (17[a])	49 (71[a])	16 (6[a])

[a] The experimental Q_n is taken from NMR results in Ref. [66].

3.2.3 Discussion

The transferability to several systems is usually a limitation of empirical potentials, that is, their parameterization should virtually be adjusted for each composition. For instance, while the widely used BKS potential[29] offers a good representation of the structure of silica, it is out-performed by the Teter potential for sodium silicate compositions[53]. On the other hand, the Teter potential would fail to predict, e.g., a correct density for glassy silica. This is especially problematic for glasses, which, as

opposed to crystals, do not have to fulfill stoichiometry rules, so that an infinite number of compositions are possible. This renders compositional studies of special interest, which requires the transferability of the potentials that are used.

In contrast, the fact of accounting for the environment for each atom renders ReaxFF transferable to various compositions. This is demonstrated by the ability of ReaxFF to model sodium silicate and glassy silica with a constant set of parameters. First, we note that ReaxFF succeeds to predict the destabilization, i.e., the elongation of Si–O bonds induced by the addition of sodium, a feature supported both by Si K_β spectrum study[51–54] and neutron scattering[62]. Indeed, ReaxFF predicts an average Si–O bond length of 1.608 and 1.620 Å in silica and NS, respectively[64]. This results in the elongation of the O–O bonds, the average length being 2.626 and 2.641 Å in silica and NS, respectively[64], in good agreement with experimental data[62]. As mentioned before, the Teter potential, on the other hand, fails to capture such a behavior. Second, ReaxFF successfully predicts the shortening of Si–Si bonds upon addition of Na_2O in the glass, which results from a decrease of the Si–O–Si angle[37]. Indeed, the average Si–Si bond length obtained by ReaxFF is 3.077 and 3.012 Å in silica and NS, respectively[64]. Third, as seen in Figure 7, ReaxFF predicts a narrowing of the Si–O–Si bond angle distribution, the FWHM obtained being 23° and 15° for silica and NS, respectively[64] (a value of 26° was observed in pure silica through nuclear magnetic resonance[67]). Such narrowing has been suggested to occur in potassium silicate[68], in which the Si–O–Si bond angle has been found to relax toward its equilibrium position upon the addition of alkali atoms. We note that this is in agreement with the fact that the Si–O–Si inter-

tetrahedral angle corresponds to a broken topological constraint in silica, whereas this angular constraint is restored in sodium silicate glasses[69–72]. Last but certainly not least, density predicted by the Teter potential is slightly closer to the experiment value than that predicted by ReaxFF. However, ReaxFF potentials involving Na were parameterized by relying on non-disorded systems such as NaH, Na_3AlH_6, and $NaAlH_4$ phases[73]. As such, under these circumstances, we believe the deviation of properties such as density from experiment (4%) does, in fact, highlight the good transferability of ReaxFF to various phases – crystalline or discorded. All together, these results demonstrate that, thanks to its bond order dependent force field, ReaxFF offers a realistic description of the effect of the addition of alkali atoms in the base silica network, thereby rendering ReaxFF highly transferable.

In addition, as opposed to pure silica, we find that the combined classical and ReaxFF approach works well for depolymerized NS structure. At the atomic scale, switching between different force fields alters the energy landscape, which may induce the appearance of internal stress in the glass structure. Unlike silica, in which long-range rearranging is virtually impossible[64], depolymerized alkali silicate glasses, thanks to their internal degrees of freedom, can relax such stress much more easily and adapt the structure with respect to the new energy minima. As such, glassy silica, once relaxed with ReaxFF, keeps the medium range order predicted by the classical potential[64]. In contrast, sodium silicate is able to feature a relaxation of its medium range order, as demonstrated by the shift of the FSDP on the neutron structure factor (see Figure XI). The improved ability for such structural relaxation is also demonstrated by the values of

the thermal expansion and Poisson's ratio, which are higher for sodium silicate than for silica[74,75], which, again, suggests an improved ability to relax the stress induced by a load or by a change of temperature. Consequently, we observe that, in the case of sodium silicate, relaxing the glassy configuration obtained from an efficient empirical potential with a more computationally simulation method, e.g., ReaxFF or *ab initio*, represents a viable option. This flexible network, as a matter of fact, suits the ReaxFF potential well, as it causes ReaxFF to better utilize its ability of accounting for the surrounding environment of atoms, which directly results in an excellent BO/NBO proportionality and good trend of Q_n distribution. Such a combined method may also be adopted for other glass compositions with relatively flexible networks, thereby allowing high throughput ReaxFF simulations of these glasses.

Overall, the improvements in the simulated NS structure produced by ReaxFF demonstrate the benefit of adopting advanced force fields in simulations of multi-component glass. The level of agreement with experiments is encouraging, especially considering that ReaxFF can potentially include a large number of elements owing to its ability to capture various types of atomic interactions.

3.3 Conclusion

We thoroughly evaluated the structure of silica and sodium silicate glasses predicted by the ReaxFF reactive potential. Our results show that ReaxFF, owing to its elaborated bond order form, is able to offer a realistic description of the de-polymerization of the silicate network by alkali network-modifiers. We observe that ReaxFF can accurately capture the destabilization of the Si–O bonds caused by the addition of alkali modifiers,

a feature that simple classical potentials fail to reproduce. We also find that ReaxFF provides an improved description of the inter-tetrahedral angle and of the medium-range order with respect to those obtained by classical MD. Combined with the ability of reactive potentials to simulate chemical reactions, these advantageous features render ReaxFF a valuable force field for the simulations of complex multi-component glasses.

Part IV. Surface Reactivity and Hydrophilicity

A study of surface interaction with water follows the validation of the ReaxFF potential on silica and sodium silicate glasses. Here, the surface topology and its effect on surface-water interaction of silica glass is accessed.

The surface reactivity and hydrophilicity of silicate materials are key properties for various industrial applications. However, the structural origin of their affinity for water remains unclear. Here, based on reactive molecular dynamics simulations of a series of glassy silica surfaces annealed at various temperatures and subsequently exposed to water, we show that silica exhibits a hydrophilic-to-hydrophobic transition driven by its silanol surface density. By applying topological constraint theory, we show that the surface reactivity and hydrophilic/hydrophobic character of silica are controlled by the atomic topology of its surface. This suggests that novel silicate materials with tailored reactivity and hydrophilicity could be developed through the topological nanoengineering of their surface.

Despite its fundamental and practical relevance, the relationship between the composition, structure, aqueous reactivity, and affinity for water of silicate materials remains poorly understood, which limits our ability to finely tailor their hydrophilicity[76–78]. This partially arises from the complex nature of disordered silicates' atomic structure, which renders it challenging to discriminate the structural features that control reactivity to the first order from those that only show a second order effect. This can be conveniently achieved by topological constraint theory (TCT, or rigidity theory), which

reduces complex atomic networks into simpler structural trusses[79–82], thereby capturing the important atomic topology while filtering out less relevant structural details that only weakly impact certain macroscopic properties. In this framework, atomic networks are described as nodes (the atoms) that are connected to each other through mechanical constraints (the chemical bonds). Such constraints comprise the radial two-body bond-stretching (BS) and angular three-body bond-bending (BB) bonds, which maintain the bond distances and bond angles fixed around their average values, respectively[83,84]. As per Maxwell's criterion, the mechanical stability of a network depends on the balance between the number of constraints and degrees of freedom[85]. Namely, atomic networks can be flexible, stressed–rigid, or isostatic if the number of constraints per atom (n_c) is lower, larger, or equal to 3 (i.e., the number of degrees of freedom per atom in three-dimensional networks). Interestingly, recent studies have suggested that the dissolution rate of silicate glasses and crystals is controlled to the first order by their atomic topology, that is, it exponentially decreases with n_c[86–94].

4.1 Methodology

Preparation of bulk glassy silica

A bulk silica glass was generated based on the common melt-quench method[95–98], as detailed in the following. First, 3000 atoms were randomly placed in a cubic simulation box while ensuring the absence of any unrealistic overlap. The system was then relaxed at 4000 K for 100 ps to ensure the loss of the memory of the initial configuration. The melt was subsequently cooled from 4000 to 300 K with a cooling rate of 1 K/ps. Finally, the glass was further equilibrated at 300 K for 1 ns. The *NPT* ensemble, ensuring a zero

pressure, was applied throughout the process. Note that, although the cooling rate used herein is much higher than those achieved experimentally, the structure of silica has been shown to weakly depend on the cooling rate[99–101]. As shown in Figure 18, the structure of glassy silica predicted by ReaxFF is in excellent agreement with neutron diffraction data[96,102].

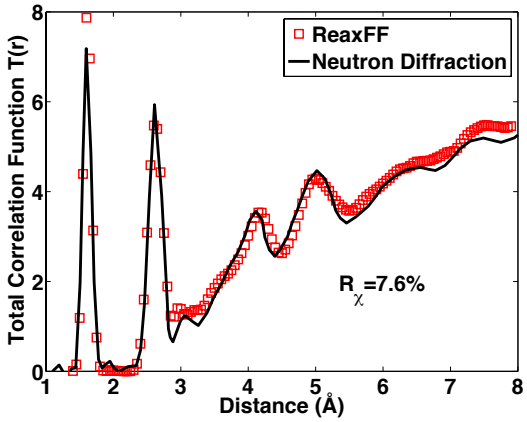

Figure 18: Total correlation function of bulk silica computed with ReaxFF. The results are compared with neutron diffraction data[102].

Preparation of the silica surfaces

Starting from the bulk glassy silica sample previously generated, two surfaces were created by instantly elongating the simulation box along the *z*-axis by 15 Å on both sides, thereby resulting in the creation of void spaces above and below the simulated system. Such distance ensures that the two surfaces do not "see" each other. The system was subsequently equilibrated at 300 K for 1 ns in the *NVT* ensemble. Next, the system was independently annealed at 700, 1000, 1300, and 1600 K for 1 ns in the *NVT* ensemble—to preserve the void space in between the two surfaces. Note that these temperatures remain low as compared to the simulated glass transition temperature (around 3000 K[97]). In all cases, this duration was found to be long enough to achieve the convergence of the pressure and energy of the system.

Preparation of the silica–water interfaces

For each annealed silica system, a silica–water interface was generated by inserting some water molecules into the void space with a density of 1 g/cm^3 (see Figure 19). The silica–water system was first subjected to an energy minimization and subsequently allowed to react at 300 K for 1 ns. During this process, the lateral dimensions (*x* and *y*) were kept fixed while a zero stress was imposed on the *z*-direction.

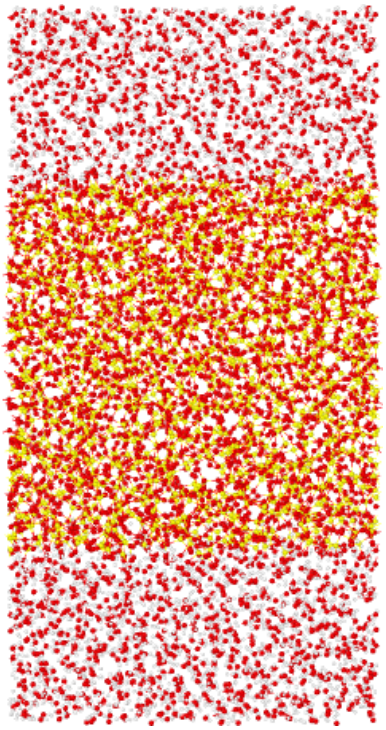

Figure 19: Illustration of the atomic configuration of a silica–water system. Si, O, and H are represented in yellow, red, and white, respectively.

4.2 Results

Structural defects at the silica surface

Starting from the basic structure of bulk silica—wherein tetrahedral Si units are connected to each other through their four corners, i.e., through BO atoms—silica's surface exhibits various structural defects, including 3-fold coordinated Si atoms (Si^{III}), terminating NBO, and edge-sharing (ES) Si units (i.e., two-membered Si ring)[103–105]. We

observe an equal concentration of NBO and Si^{III} defects, as the breakage of a Si–O bond results in the simultaneous formation of both of these defects (i.e., one on the upper surface and one on the lower surface). As shown in Figure **20**a, the surface density of NBO decreases monotonically with increasing annealing temperature. This suggests that thermal annealing partially allows the atoms to locally reorganize and relax some of the structural defects by mutual recombination of NBO and Si^{III} defects, in agreement with previous results[106–108]. This reorganization partially induces the formation of ES units, which concentration is found to increase with increasing annealing temperature (see Figure **20**b).

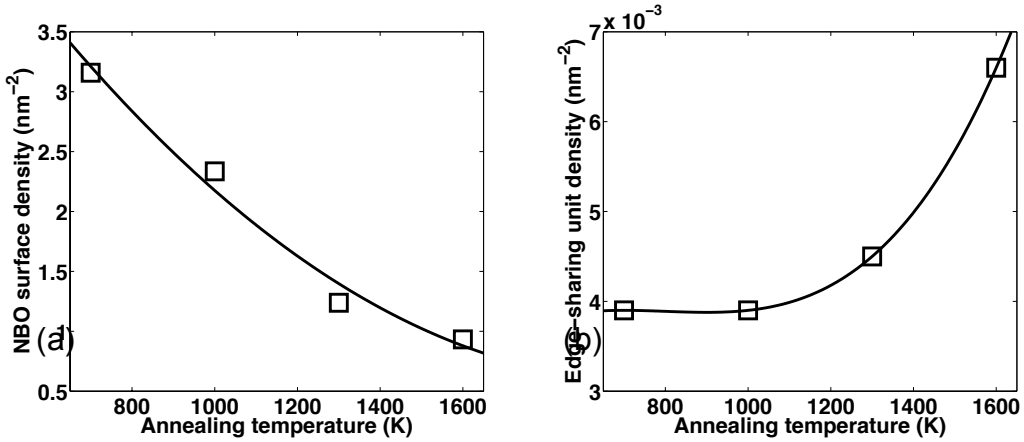

Figure 20**: Surface density of (a) non-bridging oxygen (NBO) atoms and (b) edge-sharing (ES) units as a function of the annealing temperature. The lines are guides for the eye.**

The surface energy of the silica samples was estimated from the difference of potential energy of the bulk and cut system, divided by the created surface area. In all cases, the potential energy was determined after energy minimization—to remove any thermal contribution to the computed energies. The obtained surface energy values are found to be within the range of available experimental values[109–111]. As shown in Figure 21, we observe that the surface energy decreases with increasing annealing temperature. This confirms that, when subjected to thermal annealing with increasing temperatures, the

silica surface becomes more stable and achieves a more energetically-favorable structure. In other words, an increase in the annealing temperature results in a decrease in the fictive temperature of the glass surface.

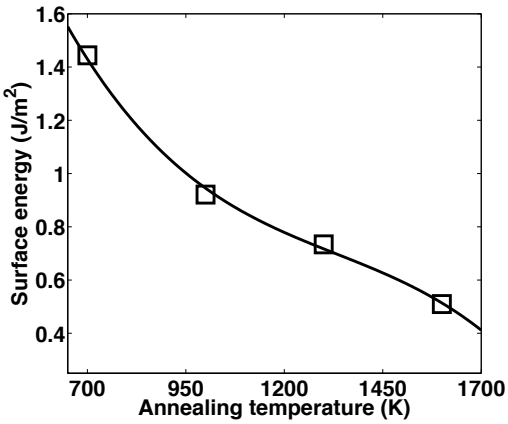

Figure 21: Surface energy of silica as a function of the annealing temperature. The line is a guide for the eye.

Formation of silanol groups upon hydration

After contact with water, we observe that some H atoms diffuse within the silica glass and form a partially hydrated layer with a depth of around 4 Å (see Figure 22a), which induces a structural reorganization of the silica surface, in agreement with previous simulations[112–115]. Si–OH silanol groups are found to quickly form (within the first picoseconds after contact with water). In the case of the as-cut silica, i.e., with no thermal annealing, the silanol surface density is found to plateau at around 5.8 nm^{-2}. This agrees well with the range of values (from 4 to 6 nm^{-2}) observed experimentally[116–118] and in previous simulations[114,119]. As shown in Figure 22b, we observe that the surface density of silanol groups decreases with increasing annealing temperature. This observation is in agreement with the outcomes of experiments performed on annealed silica samples[117,118,120,121]. This demonstrates that silica's surface reactivity decreases upon annealing, due to the relaxation of high-energy surface defects.

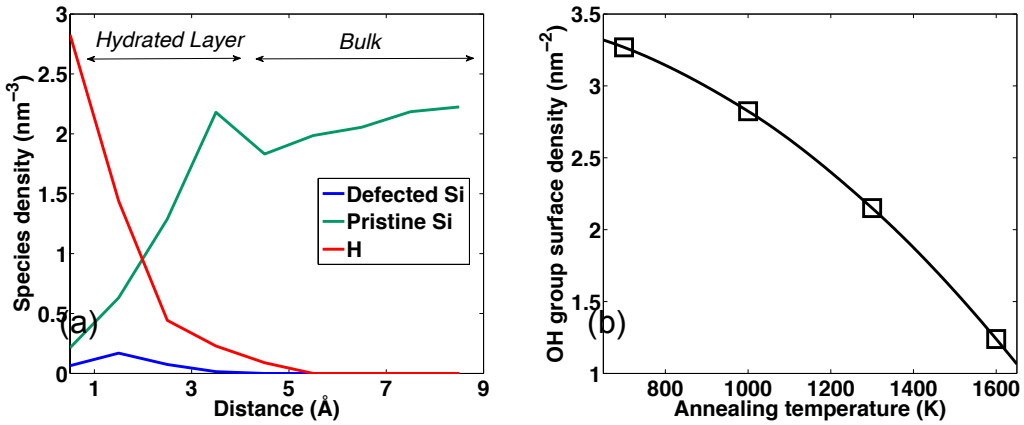

Figure 22: (a) Density profile of 4-fold Si (pristine Si), 3-fold Si (defected Si), and H atoms as function of the distance from the silica–water interface (in the absence of annealing). (b) Silanol surface density as a function of the annealing temperature. The line is a guide for the eye.

From hydrophilic to hydrophobic

To assess the affinity of the hydroxylated silica surfaces with water, the undissociated water molecules were manually separated from the surface by inserting a void space between the silica surface and the water. Note that the silanol groups formed during hydration were still attached to the surface. The difference of potential energy, before and after separation of the water from the silica surface, was used to calculate the silica–water interface energy (or binding energy), which offers a direct estimation of the level of hydrophilicity of the silica surfaces. As shown in Figure 23, we note that the interface energy decreases with increasing annealing temperature. This shows that, although it is largely hydrophilic without any thermal treatment, silica becomes significantly more hydrophobic as its surface becomes more stable and exhibit fewer structural defects.

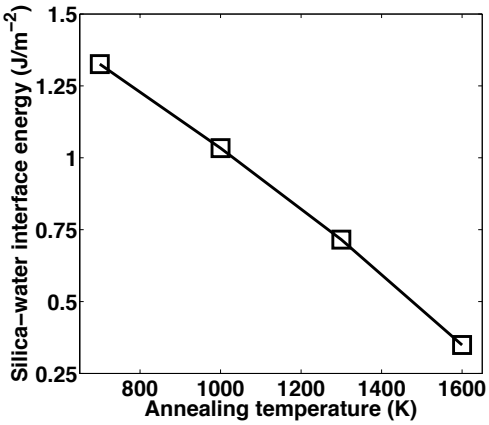

Figure 23: Silica–water interface (binding) energy as a function of the annealing temperature.

4.3 Discussion

We now investigate the relations between structural defects, silanol density, and hydrophilicity. First, as shown in Figure 24a, we observe a positive linear correlation between the silica–water interface energy and the silanol surface density. This strongly supports the idea that the hydrophilicity of silicates is primarily controlled by the number of silanol groups per unit of surface. This can be understood from the fact that silanol groups can interact with polar water molecules through the formation of hydrogen bonds (H-bonds), whereas BO (siloxane groups) are intrinsically hydrophobic[106,108,121]. Namely, if the silanol groups are, on average, close enough to each other, each water molecule will create two H-bonds with the silica surface (hydrophilic surface), whereas, if the silanol groups are far from each other, only one H-bond per water molecule will be created (hydrophobic surface)[122]. By extrapolation, we find that silica would become fully hydrophobic (i.e., negative silica–water interface energy) for a silanol surface density of around 0.5 nm^{-2}. This is in agreement with previous simulation data[108] suggesting a hydrophilic-to-hydrophobic transition occurring between 0 and 3.7 OH nm^{-2}.

Finally, we investigate how the silanol surface density and, consequently, silica's hydrophilicity is controlled by the atomic topology of the surface. In the absence of any defects, Si and O atoms create 2 and 1 BS constraints, respectively (note that each BS constraint is shared by two atoms so that the number of BS constraints created by a given atom is equal to half of its coordination number). In addition, Si atoms create 5 BB constraints, which corresponds to the 5 independent angles that need to be fixed to define the Si tetrahedra. In contrast, O atoms do not create any BB constraints due to the large angular flexibility of the Si–O–Si bond angles[84,123–125]. This leads to an isostatic structure, i.e., n_c = 3 (see enumeration in **Error! Reference source not found.**). In turn, the presence of structural defects (e.g., Si^{III} or NBO) tend to decrease the rigidity of the surface as compared to that of the pristine bulk.

To understand the linkages between surface topology and reactivity, we computed a "*surface number of topological constraint per atom*" n_c^*, that is, the average number of topological constraints per atom of the surface before exposure to water. Note that the surface is here defined as a slab ranging from z = 0 to 4 Å, where z is the distance from the silica–water interface (see Figure 24a). Rather than only considering the rigidity of the "skeleton network," that is, wherein terminating atoms are ignored, we explicitly accounted for all the atoms of the network herein (i.e., by including terminating O atoms in the constraints enumeration). Indeed, it was shown that, although the two enumeration schemes predict the same isostatic threshold (n_c = 3), the explicit incorporation of 1-fold coordinated atoms into the constraints enumeration offers a more

accurate description of the glass rigidity in the flexible (n_c < 3) and stressed–rigid domains (n_c > 3)[126,127].

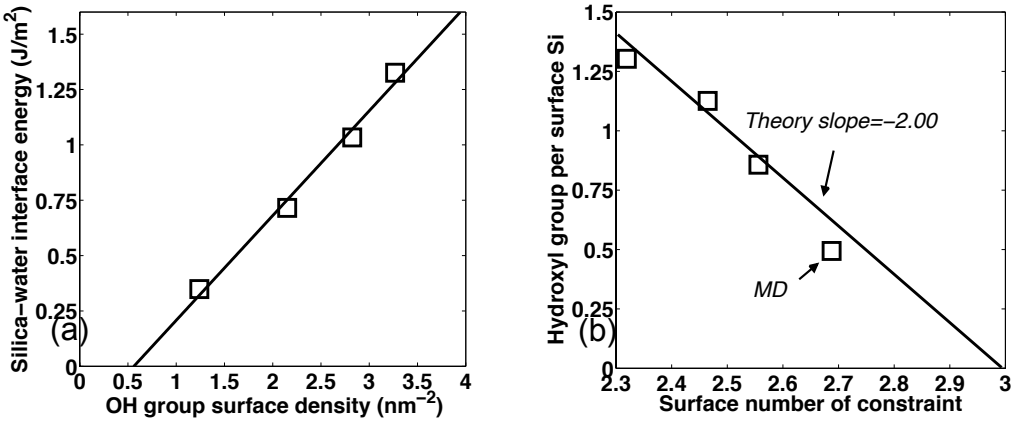

Figure 24 (a) Silica–water interface energy as a function of the surface density of silanol groups. The line is a linear fit. (b) Number of silanol groups per surface Si atom as a function of the surface number of constraints per atom n_c^*. The line is a theoretical prediction (no fitting parameters, see text).

Figure 24b shows the number of silanol group per Si atom (limited to the Si atoms belonging to the surface) as a function of the surface number of constraints per atom n_c^*. We observe that the number of silanol groups per Si atom decreases fairly linearly with n_c^* and eventually becomes zero when $n_c^* = 3$. This can be understood as follows. The $n_c^* = 3$ threshold corresponds to the value obtained for pristine silica, that is, when the atomic network is fully polymerized and only comprise hydrophobic siloxane groups. In this situation, silica does not exhibit any "open" chemisorption site for water molecules to dissociate into hydroxyl groups. Starting from this ideal network, the breakage of a Si–O bond can be expressed as the following reaction $2Q^4 \rightarrow Si^{III} + Q^3$, where a Q^n unit is defined as a 4-fold coordinated Si atom connected to *n* other Si units (i.e., comprising 4 – *n* terminating O atoms) and Si^{III} being a 3-fold coordinated Si (E' center) connected to 3 other Si units (i.e., with 3 BO atoms). As summarized in **Error! Reference source not found.**, this reaction induces the loss of 3 constraints (1 BS and 2 BB). In turn, the resulting Si^{III} and Q^3 defects offer two potential additional chemisorption sites for silanol groups. After normalization by the number of atoms in the surface, one gets the

following expression for the number of potential silanol groups per Si atom in the surface OH/Si:

$$\mathbf{OH/Si = 2(3 - n_c^*)} \qquad \textbf{Equation 6}$$

As shown in Figure 24b, the computed number of silanol groups (after hydration) agrees very well with the prediction based on the surface number of constraints per atom offered by $\mathrm{OH/Si} = \mathbf{2}(\mathbf{3} - \boldsymbol{n}_c^*$) Equation 6 (i.e., relying on the atomic topology of the surface before hydration). This suggests that the short-term reactivity of silica (as measured by the surface density of silanol groups) can be fully predicted from the atomic topology of the unreacted surface (with no fitting parameter). In turn, since the silanol surface density offers a good estimation of silica's affinity for water (see Figure 22a), our results suggest that the atomic topology of the surface controls the hydrophilicity of silica. Namely, flexible (low n_c^* values) and more rigid (n_c^* values close to 3) surfaces are associated with hydrophilic and hydrophobic behaviors, respectively. Based on our results, we identify that the hydrophilic-to-hydrophobic transition occurs at $n_c^* = 2.9$.

Table XIII: Summary of the constraints enumeration for Q^4 (i.e., 4-fold coordinated Si atoms comprising no terminal oxygen atom), Si^{III} (i.e., 3-fold coordinated Si atoms comprising 3 BO atoms), and Q^3 units (i.e., 4-fold coordinated Si atoms comprising one terminal oxygen atom). For each type of unit, the table summarizes the coordination number (CN) of Si, the numbers of bond-stretching (BS) and bond-bending (BB) constraints per unit, the total number of constraints (BS+BB), and the number of silanol groups per Si unit. The last row indicates the variation in these quantities when a Si–O bond is broken, which results in the transformation of two Q^4 units into a Si^{III} and a Q^3 unit (see text).

Unit	CN	BS	BB	BS+BB	# Silanol

Q^4	4	4	5	9	0
Si^{III}	3	3	3	6	1
Q^3	4	4	5	9	1
$2Q^4 \rightarrow Si^{III} + Q^3$		–1	–2	–3	+2

4.4 Conclusions

Our study shows that glassy silica exhibits a hydrophilic-to-hydrophobic transition upon thermal annealing of its surface. The exposure to increasing annealing temperature results in the relaxation of some of the terminating O and undercoordinated Si structural defects, leading to a more stable and less reactive surface. The surface density of silanol groups formed upon hydration is found to be controlled by the number of topological constraints per atom of the surface before hydration. In turn, the silanol surface density dictates the hydrophilic or hydrophobic character of silica. Altogether, these results open the door toward the nano-engineering of the surface of silicate materials with tailored reactivity and hydrophilicity.

Part V. Glass Hardness

Other than surface reactivity and hydrophilicity, the mechanical property such as hardness is of high importance for designing next generation high-performing glasses. Here, the hardness of sodium silicate and the deformation mechanisms that dominate it is investigated.

Elastic properties (Young's modulus *E*, bulk modulus *K*, shear modulus *G*, and Poisson's ratio υ) are of primary interest for applications such as accelerated devices, including hard discs and surgery equipment, lightweight construction and composite materials. As such, it is of primary importance to understand and predict the relation between hardness and composition. As the number of potential glass compositions is virtually infinite, conventional brute-force experimental or simulation-based approach will not enable the development of an accurate and transferrable hardness assessment. Here, based on MD simulations of sodium aluminosilicate glasses coupled with TCT, we predict the hardness value of the glasses compared with experiments. In addition, we analyzed the fundamental driving factors that governs the hardness depends on the composition. We demonstrate that our prediction offers a good agreement to experimental data, and explained the contributions from permanent densification and shear flow using TCT.

5.1 Methodology

To observe the property trend as sodium content increase, we prepared 8 sodium silicate glass samples from 5% to 40% of soda content with 5% of increment, namely, $(Na_2O)_5(SiO_2)_{95}$, $(Na_2O)_{10}(SiO_2)_{90}$, $(Na_2O)_{15}(SiO_2)_{85}$, $(Na_2O)_{20}(SiO_2)_{80}$, $(Na_2O)_{25}(SiO_2)_{75}$,

$(Na_2O)_{30}(SiO_2)_{70}$, $(Na_2O)_{35}(SiO_2)_{65}$, $(Na_2O)_{40}(SiO_2)_{60}$. The silicate systems, made of 3000 atoms, are first formed by randomly distributing atoms inside a cubic box, while ensuring no unrealistic overlapping. The system is then melted at 4000 K for 100 ps in order to ensure the loss of the memory of the initial configuration. The silicate glass is then formed by linearly reducing the temperature from 4000 K to 300 K with a cooling rate of 1 K/ps. Even though this cooling rate is noticeably higher than typically used experimental ones, it is, based on previous studies[33–35], low enough to produce realistic glasses. The effect of the cooling rate has recently been thoroughly evaluated[36] and, although the density and thermal expansion appear to be slightly affected, most of the structural features of the glass remain unchanged. After cooling, the system is further equilibrated at 300 K for another 1 ns. The NPT ensemble, which ensures a zero pressure of the system, is applied for the entire process. Note that, for computational efficiency, the Teter potential is used through the glass formation. The structure of the obtained glass, as obtained with classical MD, is then fully characterized. In addition, the formed glass is further relaxed with the ReaxFF potential for 1 ns in the NPT ensemble at zero pressure, before structural characterization. Note that this duration of relaxation is found to be sufficient to ensure the convergence of both volume and energy. Table I shows the obtained final densities, which are both in good agreement with the experimental data[51].

All sodium silicate glass samples are subsequently deformed following the above three deformation paths in a strain-control fashion. To eliminate the rate effect, all simulations are performed using strain-controlled fixed-cell energy minimization technique. The

stress-strain response is plotted accordingly for each individual deformation path. The failure analysis identifies the conservative strain, $\left(\epsilon_{zz}^{*}, \epsilon_{yz}^{*}\right)_{ext}$, and stress $\left(\sigma_{zz}^{*}, \sigma_{yz}^{*}\right)_{int}$ at which the material fails upon loading at a particular deformation path. Since the deformation is confined in the other axial directions and is subjected to the Poisson effect, a planar stress evolves in the material while undergoing constrained biaxial deformation. The planar stress is direction-independent, $\sigma_{xx}^{*} = \sigma_{yy}^{*} = \sigma_{pl}^{*}$, due to isotropy within the intra-layer of the two crystals. Therefore, the stress tensor at failure point, $\boldsymbol{\sigma}_{int}^{*}$, can be viewed as:

$$\boldsymbol{\sigma}_{\boldsymbol{int}}^{*} = \begin{bmatrix} \boldsymbol{\sigma}_{\boldsymbol{pl}}^{*} & \mathbf{0} & \mathbf{0} \\ \mathbf{0} & \boldsymbol{\sigma}_{\boldsymbol{pl}}^{*} & \boldsymbol{\sigma}_{\boldsymbol{yz}}^{*} \\ \mathbf{0} & \boldsymbol{\sigma}_{\boldsymbol{yz}}^{*} & \boldsymbol{\sigma}_{\boldsymbol{zz}}^{*} \end{bmatrix} \qquad \textbf{Equation 7}$$

The failure stress tensor can be stated in terms of principle failure stress components $(\sigma_{I}^{*} = \sigma_{II}^{*} = \sigma_{III}^{*})$ by finding the eigenvalues of failure stress tensor. Therefore, the principle stresses can be written as:

$$\sigma_I^* = \sigma_{pl}^* \qquad \text{Equation 8}$$

$$\sigma_{II}^* = \frac{1}{2}\left(-\sqrt{\left(\sigma_{pl}^* - \sigma_{zz}^*\right)^2 + 4{\sigma_{pl}^*}^2} + \sigma_{pl}^* - \sigma_{zz}^*\right) \qquad \text{Equation 9}$$

$$\sigma_{III}^* = \frac{1}{2}\left(\sqrt{\left(\sigma_{pl}^* - \sigma_{zz}^*\right)^2 + 4{\sigma_{pl}^*}^2} + \sigma_{pl}^* - \sigma_{zz}^*\right) \qquad \text{Equation 10}$$

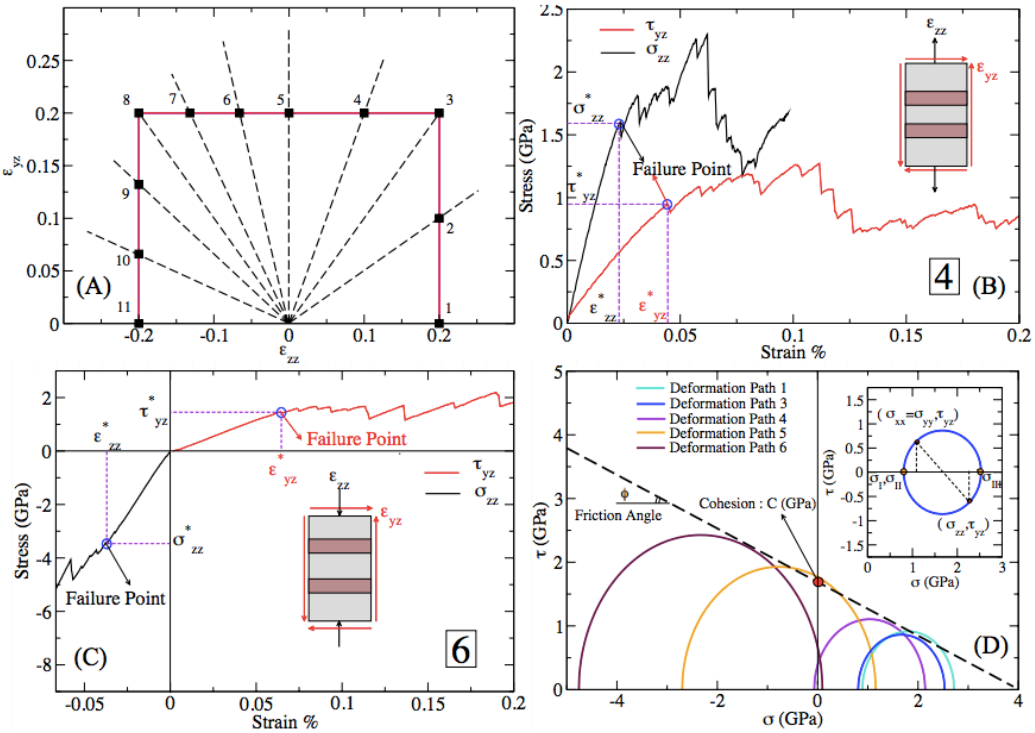

Figure 25: A set of Mohr failure circles on independent deformation paths can define the failure mechanism and the plastic limit of the material.

Using the Mohr representation, the principle components of the stress can be identified as the intersection of Mohr circles with σ-axis. The maximum and minimum of principle stresses for k^{th} deformation path are Σ_I^k and Σ_{II}^k, respectively. These two principle stresses and enclosing Mohr circles define the limit stress state at which atomic structures of the sodium silicate glass samples undergo an irreversible deformation. In Figure 25, a set of Mohr failure circles on independent deformation paths can define the failure mechanism and the plastic limit of the material. Figure 25 denotes that both crystals follow a Mohr-Coulomb-like failure criterion at the atomic scale. Application of

the Mohr-Coulomb criterion in the mechanics of disordered granular materials is prevalent due to proper description of inter-granular friction.

In particular, in the case of silicate materials, the failure envelope is linear in the stress domains relevant to the nano-indentation experiment. Therefore, silicate materials at the nano-scale can be described as a cohesive-frictional material identified via cohesion (*C*) constant and friction angle (ϕ). Cohesion is the strength of the crystal at zero confinement pressure. Following the work of Ganneau *et al.* [128], the hardness (*H*) of a cohesive-frictional material can be stated as:

$$\frac{H}{C} = \frac{\delta(\phi,\theta)}{tan\phi} = \frac{1}{tan\phi}\sum_{m=1}^{N}(a_k(\theta)tan\phi)^k \qquad \textbf{Equation 11}$$

where θ is the indenter apex angle and a_k coefficients are fitting parameters for given indenter geometry. If the friction angle is on the order of 5 degrees or less, $\tan(\phi)$ becomes negligible and as a result the hardness can be approximated with 5.8*C*. Therefore, the hardness calculated in this Part is calculated from the following:

$$H_v = 5.8C \qquad \textbf{Equation 12}$$

5.2 Results

Here, the hardness calculated for all the glass samples are plotted and compared with experimental values from indentation experiments. We observe a good agreement with the experimental values in terms of the trend, slope and the magnitude. However, it is observed that for compositions with soda content lower than 20%, the hardness H_v is slightly over-estimated. As such, sodium silicate material with soda contents lower than 20% does not appear to follow the Mohr-Coulomb criterion.

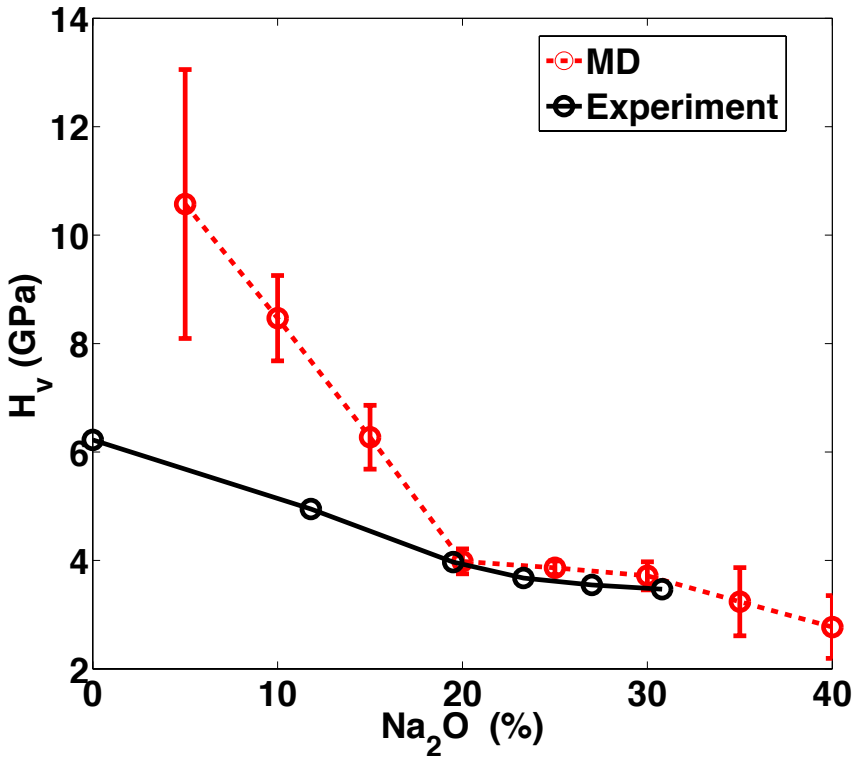

Figure 26: Hardness H_v (GPa) versus soda content in the glass samples, experimental values from indentation are plotted as well.

In order to find out the origin of this discrepancy of predicted hardness, one needs to look into the Mohr circles and their failure envelope. The Mohr circles from the various modes of deformation are plotted. The failure envelope can then be constructed based on these circles. From these circles, the cohesive strength *C* can be directly calculated from the Mohr's circles. The hardness can then be calculated. As an example, the Mohr's circle of the sodium silicate glass with 30% and 10% soda are plotted herein. It is observed that the friction angle experiences a change from negative to positive as soda content of 20%.

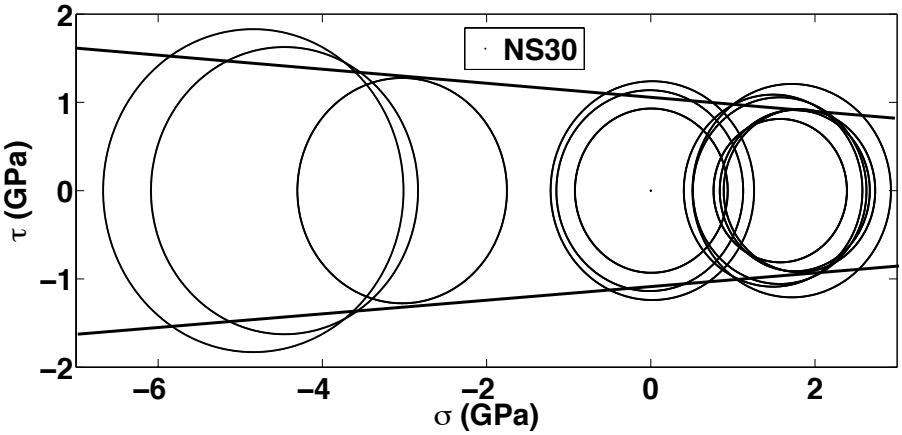

Figure 27: Mohr circles simulated with MD for sample with 30% soda content.

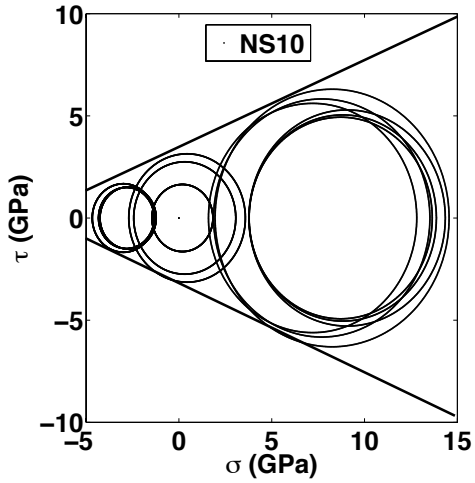

Figure 28: Mohr circles simulated with MD for sample with 10% soda content.

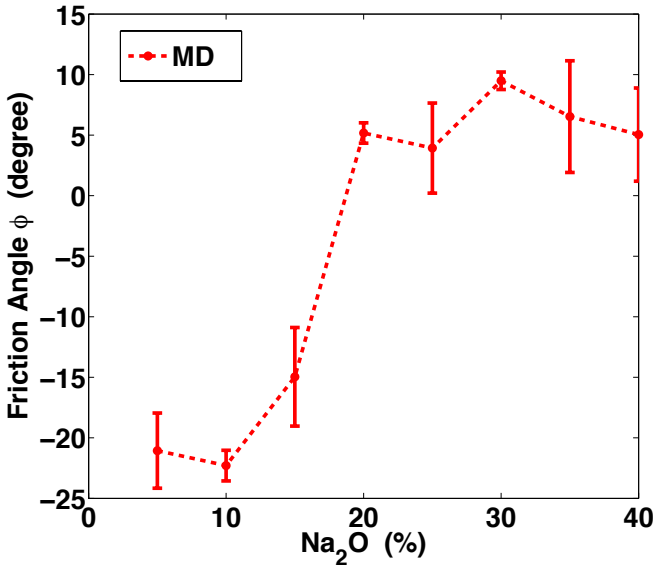

Figure 29: Friction angle versus soda content of the glass samples.

As the next step, the contributions from shear flow and densification are evaluated for all the glass samples under the deformations. It is observed that densification dominates when the soda content is lower while shear flow dominates the higher soda content glasses. It is observed that the densification increases upon the removal of Na atoms, while the plastic shear flow becomes predominant at higher Na content.

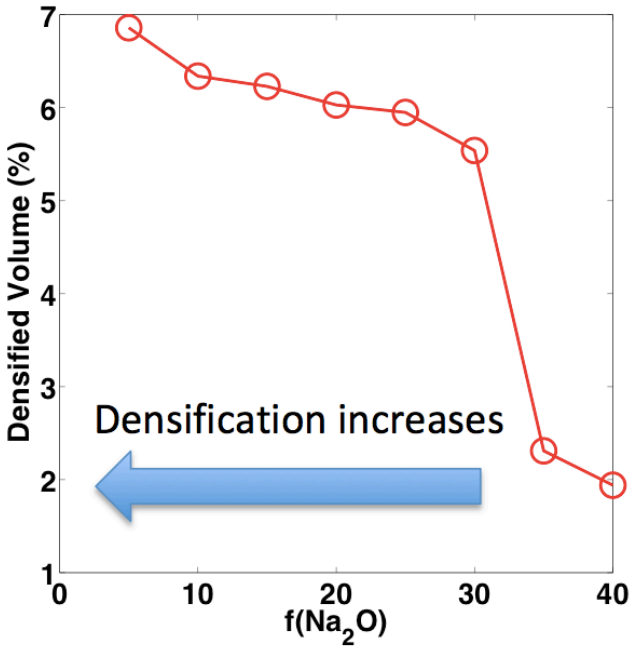

Figure 30: Percentage of permanently densified volume (%) versus soda content of the glass samples.

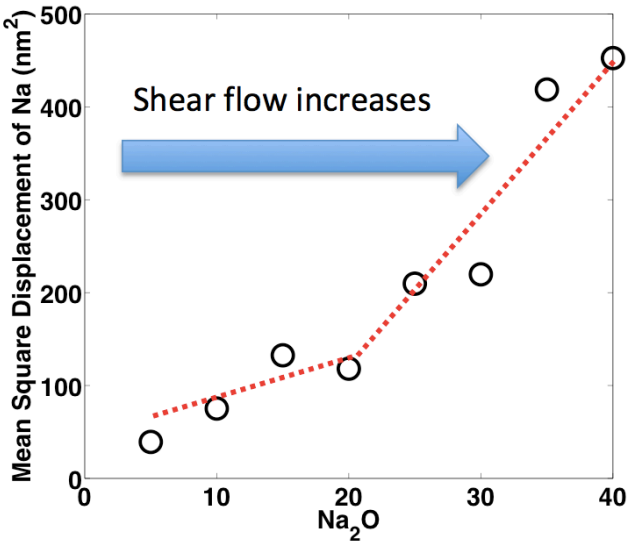

Figure 31: MSD of Na atoms (nm^2) versus soda content of the glass samples.

Topological constraint theory provides excellent explanation of the transition of dominance between densification and shear flow. Since 20% Na_2O represents the isostatic condition where the glass network is neither stressed nor over-flexible, lower Na content glasses represent stress-rigid states whereas higher Na content glasses

represent flexible states. This transition from stress-rigid to flexible is illustrated in the following figure. When a glass network is stress-rigid, the propensity for shear flow is limited by the lack of network modifier sodium; hence densification dominates the numerical value of hardness.

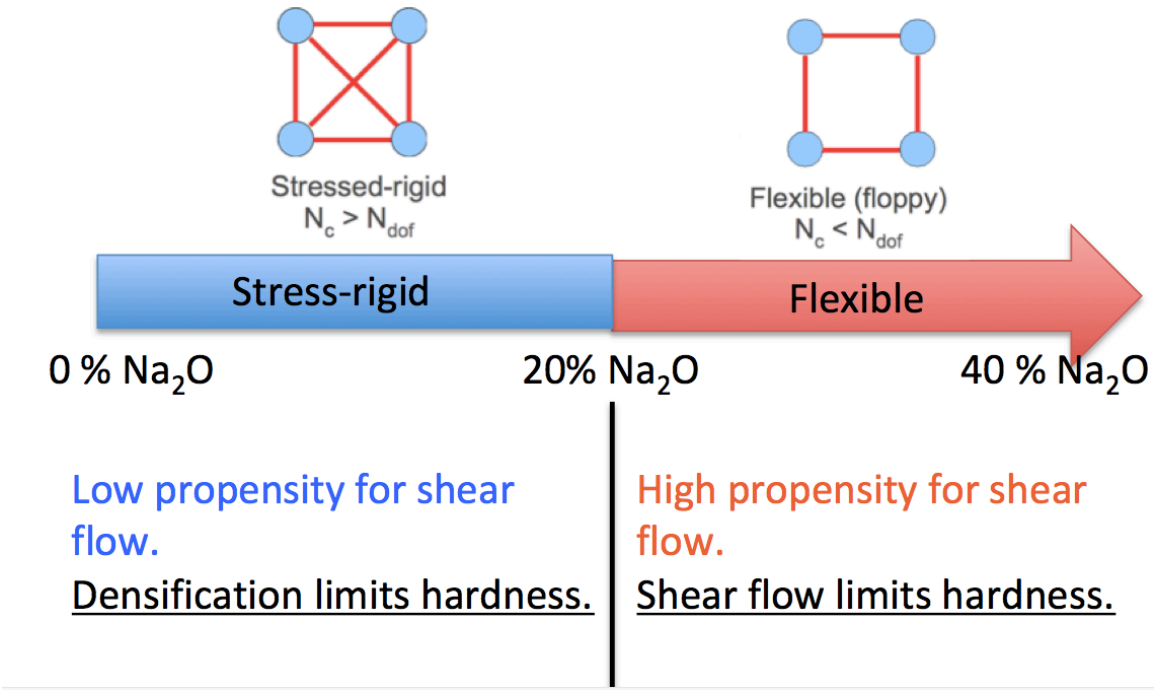

Figure 32: Transition from stress-rigid (densification dominates) to flexible (shear flow dominates).

Therefore, the anomalous behavior of the hardness can be understood in terms of the rigidity of the network. When a glass network is stressed-rigid, the residual constraint in the network makes the relaxation via shear flow difficult. On the contrary, the network tends to deform via shear flow when there is sufficient amount of network modifier to facilitate the network relaxation upon deformation.

Part VI. Mixed Modifier Effect on Hardness

To further access the hardness of complex glasses, the mixed modifier effect plays an importance role in influencing the deformation mechanism at atomic scale. This interesting composition-hardness relation brings out the atomic origin of the mixed modifier effect.

The origin and manifestations of the mixed modifier effect in silicate glasses remains poorly understood. Here, based on molecular dynamics simulations of mixed alkaline earth aluminosilicate glasses, we observe a negative deviation from linearity in hardness due to a maximum in shear flow deformations in mixed compositions. We demonstrate that the higher propensity for shear flow originates from the existence of local structural instabilities in mixed compositions due to a mismatch between the mixed modifiers and the rest of the silicate network. Overall, we suggest that the mixed modifier effect manifests itself as a competition between thermodynamic driving force for structural relaxation and kinetics thereof.

6.1 Methodology

Simulation of the glasses

To establish our conclusions, we simulated with MD a series of 17 mixed alkaline earth sodium aluminosilicate glasses $(CaO)_x(MgO)_{16-x}(Na_2O)_{12}(Al_2O_3)_{12}(SiO_2)_{60}$ mimicking the compositions considered in the work of Yue *et al.*[129] (see the list of compositions in Table XIV). For all the simulations, we relied on the well-established Pedone potential[130], as it has been shown to predict realistic mechanical properties for

aluminosilicate glasses[35,130,131]. The cutoff distance is 8.0 Å while the method for Coulombic interaction is via the Damped Shifted Force model.

Table XIV: Compositions (in mol %) of the 17 mixed alkaline earth sodium aluminosilicate glasses simulated in this study.

Ca/(Ca+Mg)	CaO	MgO	Al_2O_3	SiO_2	Na_2O
0	0	16	12	60	12
0.0625	1	15	12	60	12
0.125	2	14	12	60	12
0.1875	3	13	12	60	12
0.25	4	12	12	60	12
0.3125	5	11	12	60	12
0.375	6	10	12	60	12
0.4375	7	9	12	60	12
0.5	8	8	12	60	12
0.5625	9	7	12	60	12
0.625	10	6	12	60	12
0.6875	11	5	12	60	12
0.75	12	4	12	60	12
0.8125	13	3	12	60	12
0.875	14	2	12	60	12
0.9375	15	1	12	60	12
1	16	0	12	60	12

All glasses comprise 2990 atoms and were generated through the conventional melt-quench method[132] as follows. First, the atoms were randomly placed in a cubic box, while ensuring the absence of any unrealistic overlap. The system was then melted at 4000 K for 100 ps to ensure the loss of the memory of the initial positions. The liquids were subsequently quenched from 4000 K to 300 K with a cooling rate of 1 K/ps. Note that, although the cooling rates typically used in MD simulations are significantly higher than those typically achieved experimentally, the structure of the formed glasses typically shows a good agreement with experiments[133,35,59,60,134]. The obtained glasses

were finally further relaxed for 1 ns at 300 K. The whole process was performed within the *NPT* ensemble under zero pressure.

Hardness computation

The hardness of each glass was computed via the method introduced by Qomi *et al.* [135,136] and summarized in the following. First, all glasses were relaxed to zero temperature and pressure through an enthalpy minimization. Fifteen independent strain-controlled deformations (pure uniaxial tension/compression, pure shear, and combinations thereof) were then applied to the samples, by gradually varying the strain by increments of 10^{-4}. For each deformation, the yield point was identified from the 0.2% offset method [Ref]. The obtained shear and tensile stresses at the yield point were used to draw a Mohr's circle. The envelope of all the Mohr's circles allowed us to determine the failure limit of each sample, which was found to be well predicted by the Mohr-Coulomb failure criterion:

$$\boldsymbol{\tau = \sigma \tan(\varphi) + C} \qquad \textbf{Equation 13}$$

where τ is the failure shear stress for a given tensile stress σ, ϕ the friction angle, and C the cohesive strength. The hardness was then calculated as $H = 5.8\ C$ based finite-element results.[137] More details about this method can be found in Ref. [135] and its Supplemental Material.

Permanent densifications' contribution to hardness

The hardness of oxide glasses can typically be limited by the appearance of permanent densification and/or shear flow under the indenter tip. First, the propensity for permanent densification upon loading was assessed by subjecting the glasses to

hydrostatic compressive pressures of 10 GPa, 15 GPa, and 20 GPa. The load was applied in the *NPT* ensemble for 1 ns, which was found to be sufficient for the volume and energy of the glasses to plateau. The densified glasses were subsequently relaxed to zero pressure for another 1 ns. The extent of load-induced permanent densification was then calculated as:

$$\frac{\Delta V}{V_i} = \frac{V_i - V_f}{V_i} \qquad \textbf{Equation 14}$$

where V_i and V_f are the molar volume of the glass before and after the loading cycle, respectively.

Shear flow deformations' contribution to hardness

Second, the propensity for shear flow deformations under load was determined by applying the following methodology. Each glass sample was subjected to a shear deformation by gradually increasing the shear strain by steps of 0.2%. At each step, the energy of the system was minimized and the mean square displacement (MSD) of the atoms recorded. The final shear strain was chosen as 38%, which was found sufficient for every glass to reach their yield point. We checked that small variations in this value did not affect our conclusions. Ultimately, the system was relaxed to zero pressure. The shear flow deformations were estimated from the average final irreversible MSD of each atomic species, that is, after loading and unloading. Note that this MSD would be zero if the deformation was fully elastic, that is, if the initial position of each atom wad recovered after unloading.

Glasses' fictive temperature

The fictive temperature T_f of each glass was evaluated by cooling liquids from 4000 K to 300 K with a constant cooling rate of 1 K/ps. Every step of 100 K, 16 independent atomic configurations were selected and subsequently subjected to an energy minimization to obtain their inherent configuration—to remove the contributions of thermal vibrations in their enthalpy. The enthalpies of the inherent configurations (ground-state enthalpy H_0) were recorded and averaged for each temperature (T). The fictive temperature of each sample was then determined as the temperature at which the $H_0(T)$ curves exhibit a change of slope, which was determined by linearly fitting the low- and high-temperature parts of the $H_0(T)$ curves (see Ref. [138] or details).

Computation of the stress per atom

To assess the stability of the atomic structure, the local stress experienced by the atoms was assessed based on the virial definition of stress[139] and the Voronoi volume of each atom. The local pressure applied to each species was calculated from the trace of the stress tensor. By convention, a positive stress represents here a state of tension, whereas a negative one represents a state of compression. The reference state of stress of Ca and Mg cations was determined from the non-mixed configurations, that is, in the absence of Mg and Ca cations in the network, respectively. In the following, we define the "instability stress" as the departure of the local pressure experienced by Ca and Mg atoms with respect to their reference states of stress.

6.2 Results

Mixed modifier effect on hardness

Figure 33 shows the computed hardness of the mixed Ca–Mg glasses. We first observe that our methodology yields hardness values that are in good agreement with experiments[140], both in terms of magnitude and trend. In particular, our simulations reproduce the broad minimum of hardness that is experimentally observed for mixed compositions (i.e., within CaO/(CaO+MgO) = 0.4-to-0.7, as indicated by a grey area in Figure 33). The deviation from linearity of the hardness is a direct consequence of the mixed modifier effect[140].

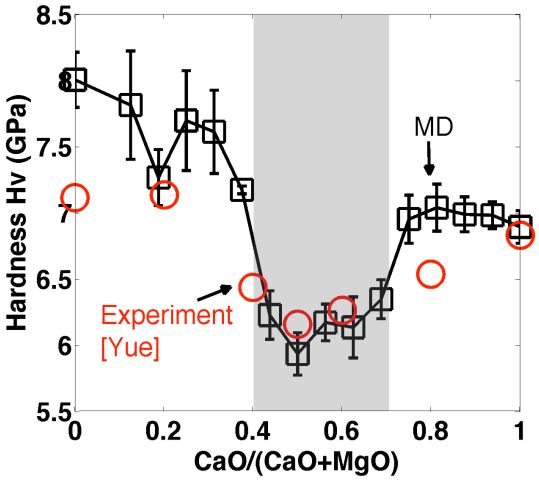

Figure 33: Computed hardness of the simulated glasses. The computed data are compared to experimental values[140]. The grey area denotes the range of compositions wherein hardness exhibits a negative deviation from linearity.

Propensity for permanent densification and shear flow

We now investigate whether the observed minimum of hardness for mixed compositions arises from an enhanced propensity for permanent densification or shear flow under load[140–143]. We first assess the extent of permanent densification of the glass samples after a hydrostatic loading/unloading cycle (see the Methods section). As shown in

Figure 34, we observe that, as expected, the extent of permanent densification increases with the applied load. However, although an appreciable amount of permanent densification is observed, we note that it remains fairly constant across all compositions. Hence, the minimum of hardness observed herein does not arise from an enhanced propensity for permanent densification. This conclusion is in agreement with previous experimental observations[140,142].

We now focus on assessing the propensity for shear flow deformations by subjecting the samples to a shear deformation followed by a relaxation to zero stress and tracking the irreversible MSD of each atom (see Methods section). Overall, we observe that only Ca and Mg cations exhibit an appreciable displacement (i.e., larger than one inter-atomic distance). The irreversible MSD of the Ca and Mg cations is shown in Figure 34(a). We observe a maximum in shear for mixed compositions feature maximum shear flow, wherein hardness shows a minimum (i.e., for CaO/(CaO+MgO) = 0.4-to-0.7). As shown in Figure 34(b), hardness linearly decreases as function of the computed shear flow. This shows that, for the glasses considered herein, the propensity for shear flow deformations controls the value of the hardness and, therefore, that the observed minimum in hardness arises from a maximum in the propensity for shear flow. This is in line with previous experimental results[140,142].

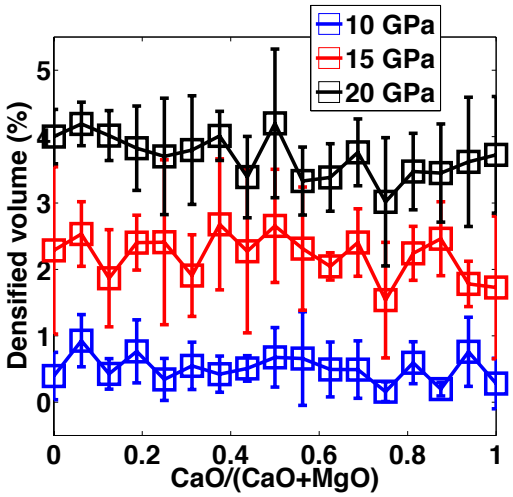

Figure 34: Fraction of permanently densified volume (see $\frac{\Delta V}{V_i} = \frac{V_i - V_f}{V_i}$ Equation 14) after hydrostatic loading under 10, 15, and 20 GPa followed by unloading to zero pressure.

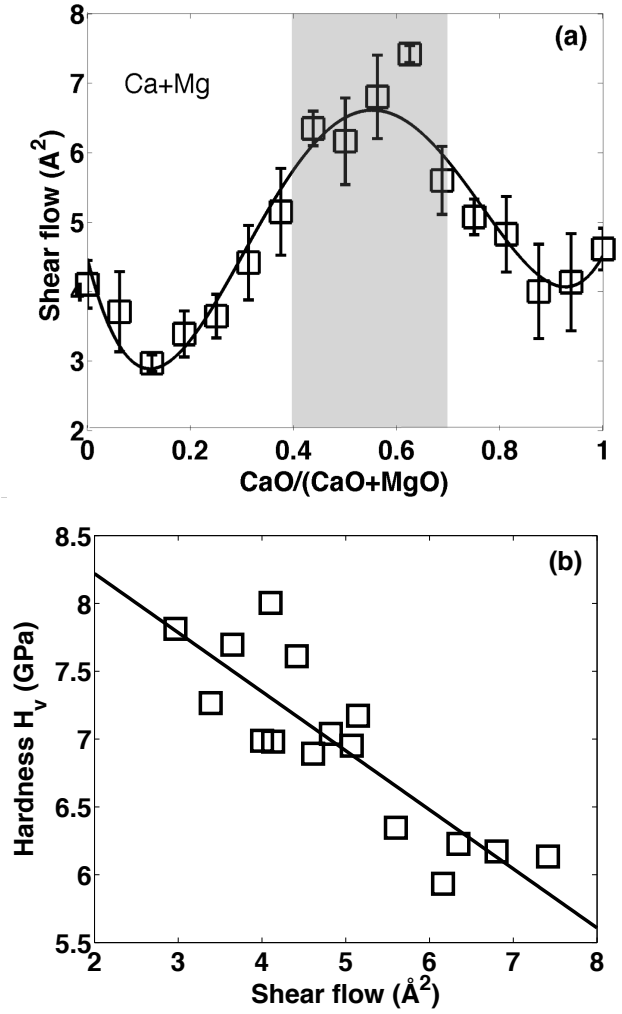

Figure 35: (a) Computed shear flow (as captured by the irreversible mean squared displacement of Ca and Mg atoms upon shearing, see Methods section). The grey area denotes the range of compositions wherein hardness exhibits a negative deviation from linearity (see Figure 33). The line serves as a guide for the eye. (b) Computed hardness (see Figure 33) as a function of shear flow. The line is a linear fit.

Origin of the mixed modifier effect on hardness

We now investigate the structural origin of the enhanced propensity for shear flow exhibited by mixed Ca-Mg aluminosilicate glasses. The observed reorganization of the Ca and Mg atoms under shear suggest the existence of local instabilities, which are released under stress—just like a granular material subjected to vibrations can reorganize itself to minimize its potential energy[144]. To quantify the stability of the atomic network, we computed the "instability stress" locally applied to each Ca and Mg atom (see the Methods section). As shown in Figure 36 (a), we observe that the average stress applied to Ca and Mg cations exhibit a clear dependence on composition. Namely, the average stress experienced by Mg cations decreases upon the addition of Ca, whereas that experienced by Ca atoms increases upon the addition of Mg, that is, Mg and Ca cations enter a state of local compression and tension in mixed compositions, respectively. Such trends have also been observed in mixed alkali silicate glasses[145].

These trends can be understood as follows. First, we note that, starting from the pure Mg aluminosilicate glass, the addition of Ca atoms results in a decrease in the fictive temperature (see Figure 36 (b), as observed experimentally[140]—note that the high cooling rate used in MD simulations result in higher fictive temperatures than those observed experimentally[138]. The observed decrease in the fictive temperature allows the formation of a denser, more optimally packed silicate network upon the addition of Ca

cations[146]. Consequently, the local spacing available to Mg cations tend to decrease upon the addition of Ca cations, thereby imposing a state of compression for Mg cations. In contrast, starting from the pure Ca aluminosilicate glass, the addition of Ca cations results in an increase in the fictive temperature, which renders the silicate backbone of the glass less efficiently packed. This induces an increase in the local spacing available to Ca cations, which thereby enter a state of tension. Overall, the local stress experienced by Ca and Mg cations results from a mismatch between these cations and the rest of the silicate network in mixed compositions.

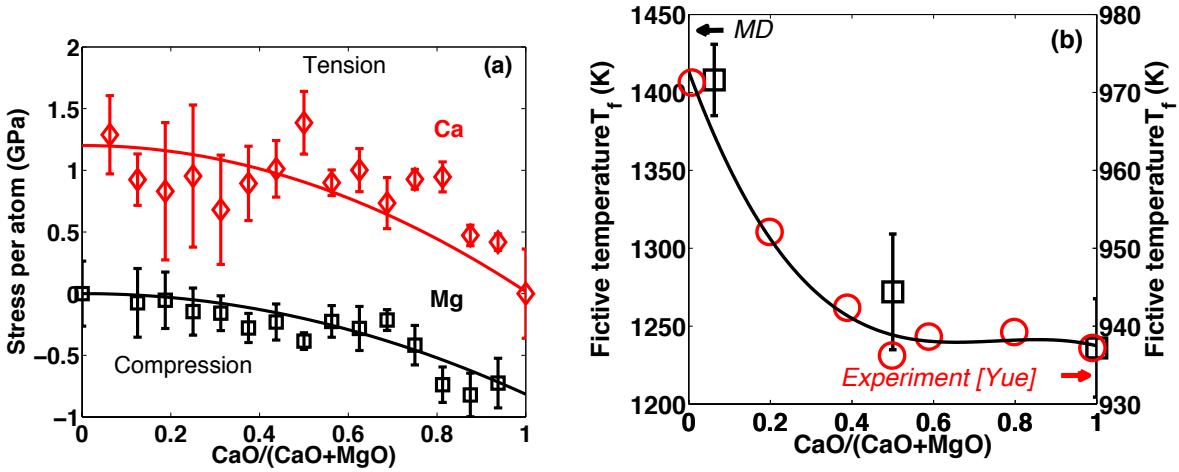

Figure 36: (a) Average "instability stress" per Ca and Mg cation. A positive (negative) stress denotes a local tension (compression). The lines serve as guides for the eye. (b) Computed fictive temperature (left axis), compared with experimental data (right axis) from Yue et al.[140].

The overall structural instability of the network then results from the balance of two competing behaviors. (1) the absolute stress per Ca or Mg cation increases upon the addition of Mg and Ca, respectively and (2) in contrast, the number of Ca and Mg decreases upon the addition of Mg and Ca, respectively. Altogether, this balance results in the existence of a maximum of in the total absolute stress applied to all Ca and Mg

cations, as shown in Figure 37(a). The overall thermodynamic driving force for shear flow can then be estimated from the difference of the total stress experienced by Ca and Mg cations. As shown in Figure 37(b), this driving force exhibits a broad maximum around CaO/(CaO+MgO) = 0.6, that is, for compositions wherein the propensity for shear flow is maximum. As shown in Figure 37(b), this driving force disappears after the glass is sheared, which further supports the fact that the enhanced propensity for shear flow originates from the local stress initially experienced by Ca and Mg atoms in mixed compositions.

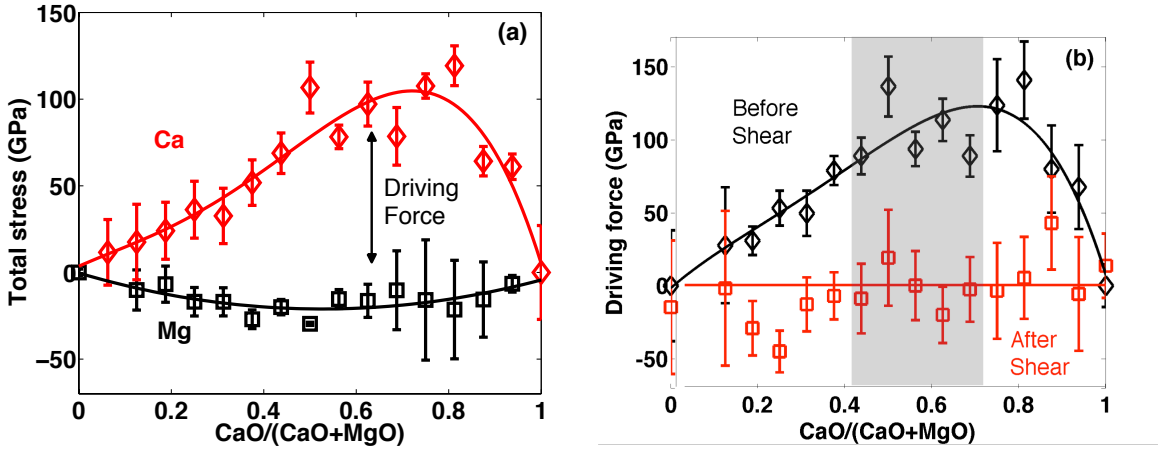

Figure 37: Total stress applied to Ca and Mg cations, prior to any shear flow. The difference between the total stress experienced by Ca and Mg cations corresponds to the thermodynamic driving force for shear flow reorganizations. (b) Driving force for shear flow, before and after shear. The grey area indicates the compositional range wherein hardness exhibits negative deviation from linearity. The lines serve as guides for the eye.

6.3 Discussion

We now discuss the impact of the mixed modifier effect on shear flow deformations under load. The link between local stress and propensity for shear flow can be understood as follows. The variation in the degree of packing of the silicate network upon the addition of Ca or Mg cations tends to deform the local energy landscape

accessible to Ca and Mg cations and render them less stable. However, the high viscosity of the glass prevents these cations from migrating to release their local stress. In turn, the application of a stress deforms the energy landscape, which allows the atoms to jump over some energy barriers (that would otherwise be too high to be overcome) to relax toward lower energy states[147]. This facilitates the jump of the cations toward other pockets within the silicate network that better fit their sizes to release their local stress. As the shear stress is removed, the atoms remain in their local pockets—so that this transformation is irreversible. Hence, the application of stress allows the system to artificially "over-age" toward more stable configurations[148].

Shear flow reorganizations upon loading then require two conditions to occur in a significant fashion: (1) a thermodynamic driving force for structural relaxation must exist and (2) if thermodynamically favorable, such relaxation should occur over the time during which the load is applied. Based on this, it becomes clear that shear flow results from the balance between (1) thermodynamic driving force and (2) kinetics. Note that the mixed modifier effect affects (1) and (2) in a competitive fashion. On one hand, as shown herein, the mixed modifier effect results in the appearance of some local stress, which acts as a driving force for relaxation. However, on the other hand, it is well known that the mixed modifier effect results in a decrease in the mobility of the network modifiers within silicate glasse[149] – which has been attributed to the fact that, due to their different sizes, the mixed modifiers mutually block each other's pathways. Overall, we conclude that the mixed modifier effect can results in an increase or a decrease in the amount of shear flow deformations, based on the competition between

thermodynamic driving force and kinetics. This competition can explain the apparently contradictory experimental observations regarding the role of the mixed modifier effect on hardness[150].

6.4 Conclusion

Overall, we observe that mixed alkaline earth aluminosilicate glasses exhibit a negative deviation from linearity in their hardness due to a higher propensity for shear flow in mixed compositions. In turn, the maximum in the propensity for shear flow is found to originate from the formation of local structural instabilities in mixed compositions, which arise from a mismatch between the modifier cations and the rest of the silicate network. More generally, we suggest that the presence of mixed modifiers has a competitive effect on the thermodynamic driving force and kinetics of atomic rearrangements under load and, therefore, can result in a positive or negative deviation from linearity in hardness.

Part VII. Mixed Modifier Effect on Relaxation

Finally, the mixed modifier effect is studied further for its influence on glasses' relaxation under low temperature. A deep similarity can be observed between mixed alkali and mixed alkaline earth effects, in terms of atomic "dissatisfaction" between competing modifiers, that is eventually reflected by composition-property relation observed in experiments.

Although it is indeed commonly believed that, as frozen supercooled liquids, glasses should continue to flow over the years (e.g., in the case of the stained-glass windows of medieval cathedrals), the dramatic increase of their viscosity below the glass transition temperature suggests, on the contrary, that their relaxation time is on the order of 10^{32} years at room temperature. However, a recent study conducted by Mauro *et al.* reported the intriguing dynamics of the relaxation of a commercial Corning® Gorilla Glass® at room temperature, over 1.5 years. Here, we report a novel atomistic simulation method allowing us to directly access the long-term (years) dynamics of glass relaxation at room temperature. Based on the simulation of a series of mixed alkali silicate glasses, we demonstrate that room-temperature relaxation is a direct consequence of the mixed alkali effect. Although both volume and energy feature a stretched exponential relaxation, our results reveal a bifurcation of the stretching exponents, with β = 3/5 and 3/7 for energy and volume relaxation, respectively. Relaxation is found to occur through the diffusion of local stressed structural instabilities inside the atomic network, which anneal each other when a compressed atomic unit meets one that is under tension. The driving force for such diffusion-trap relaxation mechanism is found to be at a maximum

when the concentrations of each alkali atom equals each other, which arises from a balance between the concentration of each alkali atom and the magnitude of the local stress that they undergo.

7.1 Methodology

Here, to investigate the MAE in glass relaxation, we simulated using molecular dynamics (MD) a series of $(K_2O)_x(Na_2O)_{16-x}(SiO_2)_{84}$ (mol %) mixed alkali silicate glasses, made of 2991 atoms, with varying *x*. All MD simulations were performed using the well-established Teter potential [151–153] with an integration timestep of 1 fs. Coulomb interactions were evaluated by the Ewald summation method with a cutoff of 12 Å. The short-range interaction cutoff was chosen as 8.0 Å. Liquids were first generated by placing the atoms randomly in the simulation box. The liquids were then equilibrated at 5000 K in the *NPT* ensemble for 1 ns, at zero pressure, to assure the loss of the memory of the initial configuration. Glasses were formed by linear cooling of the liquids from 5000 to 0 K with a cooling rate of 1 K/ps in the *NPT* ensemble at zero pressure.

To simulate the long-term relaxation of these glasses, we relied on a new accelerated simulation technique that we recently developed to understand the origin of room-temperature relaxation in Corning® Gorilla® Glass [154,155]. In that method, the simulated glass is subjected to small, cyclic perturbations of volumetric stress. This method mimics the relaxation observed in granular materials subjected to vibrations [156], wherein small vibrations tend to densify the material (artificial aging), whereas large vibrations randomize the grain arrangements (rejuvenation). Similar ideas, relying on the energy landscape approach [157], have been applied to non-crystalline solids, based on the fact

that small stresses deform the energy landscape locally explored by the atoms. This can result in the removal of some energy barriers that exist at zero stress, thus allowing the system to jump over the barriers to relax to lower energy states. More details about this method can be found in Ref. [155].

As expected, the stress perturbations allow all glasses to relax towards lower energy states [155]. As shown in Figure 38, all glasses also show a gradual compaction in volume upon relaxation. Remarkably, the volume relaxation observed herein follows a stretched exponential decay function that is similar to that observed experimentally [154]. Further, we observe that the mixed $(K_2O)_8(Na_2O)_8(SiO_2)_{84}$ glass (denoted Na+K thereafter) features a larger densification than the binary sodium and potassium silicate glasses (denoted Na and K thereafter). This is a clear demonstration that the thermometer effect is indeed a manifestation of the MAE.

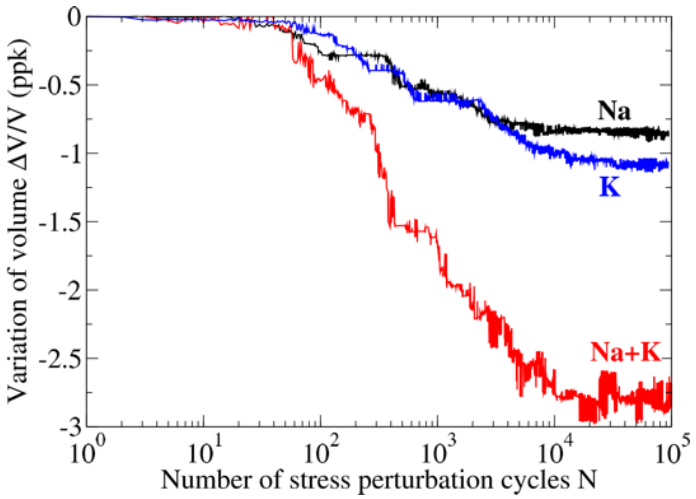

Figure 38: Relative variation of the volume of the sodium (Na), potassium (K), and mixed alkali (Na+K) silicate glasses with respect to the number of stress perturbation cycles applied. Lines serve as guide for the eye.

7.2 Results

We now investigate the origin of the MAE in the context of relaxation. The stretched exponential nature of glass relaxation can be predicted by the Phillips' diffusion-trap model, wherein "excitations" in the glass diffuse toward randomly distributed "traps" [158]. However, this model remains largely axiomatic. Here, we propose that the excitations introduced within the diffusion-trap model correspond to locally unstable atomic units.

To assess this hypothesis, we first computed the coordination number (CN) of all atomic species. As shown in Figure 39a, the CN of Na decreases upon the addition of K, whereas that of K increases upon the addition of Na, which can be attributed to a mismatch between the alkali atoms of the rest of the silicate network as one moves away from the binary composition. This miscoordinated state results in the formation of local stresses inside the atomic network, which was assessed by computing the local stress applied to each atom [159]. As shown in Figure 39b, the average stress

experienced by Na atoms increases upon the addition of K, whereas that experienced by K atoms decreases upon the addition of Na. This can be understood as follows. Over-coordinated K atoms present an excess of O atoms in their first coordination shell. Due to mutual repulsion, O atoms tend to separate from each other, which, in turn, tends to stretch the K–O bonds. On the other hand, under-coordinated Na atoms show a deficit of O atoms, which, in turn, are more attracted by the central cation. This results in a compression of Na–O bonds.

The mechanism of glass relaxation can then be understood as follows. Miscoordinated species act as local instabilities (or “excitations” following Phillips terminology). These excitations diffuse via local deformations of the atomic network, until an atomic arrangement that is locally under compression meets one that is under tension. At this point, both excitations are annihilated (or reach a “trap”), thereby relieving the initial internal stress stored in the network. The driving force for relaxation corresponds to the difference between the total cumulative stress experienced by Na and K atoms, which arises from the balance between two competitive behaviors. (1) The absolute stress per atom experienced by Na and K species increases upon the addition of K and Na, respectively. (2) In contrast, the numbers of Na and K atoms present in the network decreases upon their replacement by K and Na atoms, respectively. Altogether, as shown in Fig. 2c, the total cumulative stress experienced by Na and K atoms reaches a maximum when the number of Na equals that of K. This behavior provides an intuitive atomistic origin of the excessive volumic relaxation of glasses comprising mixed alkali atoms (i.e., thermometer effect).

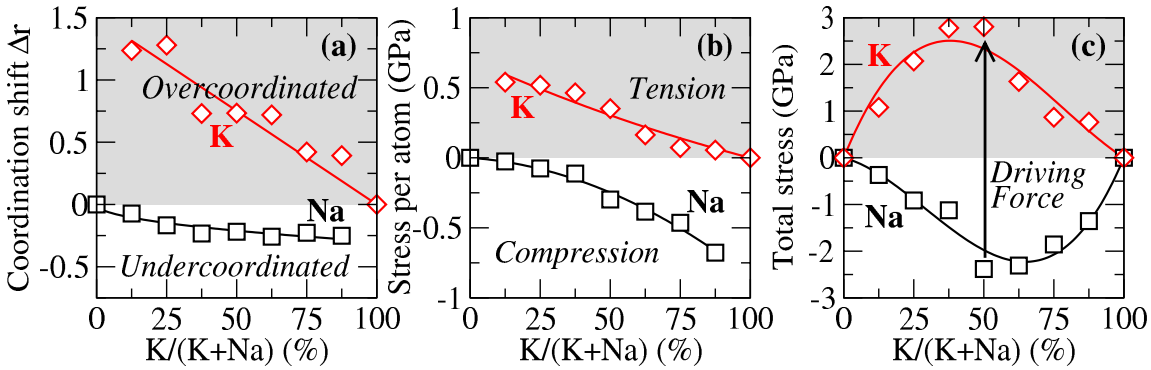

Figure 39: (a) Shift of the coordination number of Na (K) atoms, using the binary sodium (potassium) silicate glass as a reference, with respect to the composition of the glass. (b) Average stress per Na and K atoms. A positive (negative) stress denotes a local compression (tension). (c) Total cumulative stress experienced by all Na and K atoms. Lines serve as guides for the eye.

7.3 Conclusions

In future work, we plan to extent our analysis to mixed alkaline earth silicate glasses to assess the generality of the present results. Besides relaxation, we also plan to investigate the effect of the local atomic instabilities evidenced herein on the mechanical properties of glasses.

Part VIII. Conclusions and Outlooks

8.1 Mechanical Property

The following have been accomplished during the course of the study:

- Validation of MD potentials.
- Elucidating composition to mechanical property relations.
- Origin of compositional influence on mechanical properties.

MD simulations are applied to enumerate the number of constraints in silicate glasses. While I rely on MD simulations to get relevant structural information for this analysis, it should be noted that my goal herein is to develop predictive models that will allow elucidation of composition-mechanical property relations, without the need of MD simulations, for a wide-range of glass compositions. Therefore future work includes:

(i) Confirm the origin of mixed modifier effect in various other silicate glass compositions.

(ii) Establish model for more complex silicate glass compositions, based on the physical origin of the mechanical property-composition relation.

(iii) Nano-indentation experiment for validating constructed model.

8.2 Reactivity and Hydrophilicity

During the study, following steps have been accomplished.

- Validation of reactive potential (ReaxFF potential) on silica (base material for silicate glasses), sodium silicate/sodium aluminosilicate glasses (more complex with network-modifiers).

- Validation study of hydration with ReaxFF. Study carried out with silica, where experimental data of surface hydroxyl group (OH^-) density is abundant.
- Access the surface topology to hydrophilicity relation
- Constructing model predicting surface hydrophilicity with TCT.

Strategies to implement topological constraint theory using molecular dynamics is:

i) Analyze atomic network using topological constraint theory,

ii) Relate available reactivity data to the TCT analysis,

iii) Examine and validate the performance of fly ashes or C_3S in relation to TCT metric,

iv) Exploit new knowledge gained in previous steps.

A clear relationship between the composition and the reactivity of is established. Therefore with the future outcomes, one should be able to:

(iv) Enhance the use of the model for more complex silicate glass compositions.

(v) Enhance the use of supplementary cementitious material (SCM) by better proportion high-volume fly ash (HVFA) binders.

(vi) Better understand the most reactive phase in ordinary Portland cement (OPC); establish the relationship between the electronic property and the long-term hydration behavior.

8.3 Relaxation

The study of relaxation of glasses at low temperature is of fundamental and practical interest. With the preliminary simulation results, I extend my study to understanding the origin of relaxation systematically, and examine the effect from the composition.

Interestingly, it is observed that a potassium sodium aluminosilicate glass relaxes the most when potassium content equals sodium content[160]. In particular, relaxation has been shown to be fastest for isostatic systems, which are characterized by an atomic network rigid but free of internal stress. This brings forward an intriguing study that relates the rigidity of the network to the glass relaxation. Beyond glasses, being able to predict and tune the relaxation and aging of materials could improve the understanding of memory-encoded materials. Here, a series of potassium sodium aluminosilicate glass are explored and their atomic structures are categorized according to TCT metrics. Thereafter, a model that governs the relaxation phenomenon is put forward based on the TCT category.

Bibliography

1. Delaye, J.-M., Cormier, L., Ghaleb, D. & Calas, G. Investigation of multicomponent silicate glasses by coupling WAXS and molecular dynamics. *J. Non-Cryst. Solids* **293–295,** 290–296 (2001).

2. van Duin, A. C. T. *et al.* ReaxFFSiO Reactive Force Field for Silicon and Silicon Oxide Systems. *J. Phys. Chem. A* **107,** 3803–3811 (2003).

3. Tersoff, J. Empirical interatomic potential for silicon with improved elastic properties. *Phys. Rev. B* **38,** 9902–9905 (1988).

4. Brenner, D. W. Empirical potential for hydrocarbons for use in simulating the chemical vapor deposition of diamond films. *Phys. Rev. B* **42,** 9458–9471 (1990).

5. Kim, K. *et al.* Ripping Graphene: Preferred Directions. *Nano Lett.* **12,** 293–297 (2012).

6. Jensen, B. D., Bandyopadhyay, A., Wise, K. E. & Odegard, G. M. Parametric Study of ReaxFF Simulation Parameters for Molecular Dynamics Modeling of Reactive Carbon Gases. *J. Chem. Theory Comput.* **8,** 3003–3008 (2012).

7. Mueller, J. E., van Duin, A. C. T. & Goddard, W. A. Development and Validation of ReaxFF Reactive Force Field for Hydrocarbon Chemistry Catalyzed by Nickel. *J. Phys. Chem. C* **114,** 4939–4949 (2010).

8. Norman, P. *et al.* The Structure of Silica Surfaces Exposed to Atomic Oxygen. *J. Phys. Chem. C* **117,** 9311–9321 (2013).

9. Kim, S.-Y. *et al.* Development of a ReaxFF Reactive Force Field for Titanium Dioxide/Water Systems. *Langmuir* **29,** 7838–7846 (2013).

10. Raju, M., Kim, S.-Y., van Duin, A. C. T. & Fichthorn, K. A. ReaxFF Reactive Force Field Study of the Dissociation of Water on Titania Surfaces. *J. Phys. Chem. C* **117,** 10558–10572 (2013).

11. Zhang, Q. *et al.* Adhesion and nonwetting-wetting transition in the Al/α -Al2O3 interface. *Phys. Rev. B* **69,** 045423 (2004).

12. Abdolhosseini Qomi, M. J. *et al.* Combinatorial molecular optimization of cement hydrates. *Nat. Commun.* **5,** (2014).

13. Bauchy, M., Abdolhosseini Qomi, M. J., Bichara, C., Ulm, F.-J. & Pellenq, R. J.-M. Nanoscale Structure of Cement: Viewpoint of Rigidity Theory. *J. Phys. Chem. C* **118,** 12485–12493 (2014).

14. Bauchy, M., Qomi, M. J. A., Ulm, F.-J. & Pellenq, R. J.-M. Order and disorder in calcium–silicate–hydrate. *J. Chem. Phys.* **140,** 214503 (2014).

15. Bauchy, M. *et al.* Fracture toughness of calcium–silicate–hydrate from molecular dynamics simulations. *J. Non-Cryst. Solids* **419,** 58–64 (2015).

16. Theofanis, P. L., Jaramillo-Botero, A., Goddard, W. A. & Xiao, H. Nonadiabatic Study of Dynamic Electronic Effects during Brittle Fracture of Silicon. *Phys. Rev. Lett.* **108,** 045501 (2012).

17. Buehler, M. J., Tang, H., van Duin, A. C. T. & Goddard, W. A. Threshold Crack Speed Controls Dynamical Fracture of Silicon Single Crystals. *Phys. Rev. Lett.* **99,** 165502 (2007).

18. Bauchy, M., Qomi, M. J. A., Bichara, C., Ulm, F.-J. & Pellenq, R. J.-M. Rigidity Transition in Materials: Hardness is Driven by Weak Atomic Constraints. *Phys. Rev. Lett.* **114,** 125502 (2015).

19. Fogarty, J. C., Aktulga, H. M., Grama, A. Y., Duin, A. C. T. van & Pandit, S. A. A reactive molecular dynamics simulation of the silica-water interface. *J. Chem. Phys.* **132,** 174704 (2010).

20. Rimsza, J. M., Deng, L. & Du, J. Molecular dynamics simulations of nanoporous organosilicate glasses using Reactive Force Field (ReaxFF). *J. Non-Cryst. Solids* (2016). doi:10.1016/j.jnoncrysol.2015.04.031

21. van Duin, A. C. T., Dasgupta, S., Lorant, F. & Goddard, W. A. ReaxFF: A Reactive Force Field for Hydrocarbons. *J. Phys. Chem. A* **105,** 9396–9409 (2001).

22. Rappe, A. K. & Goddard, W. A. Charge equilibration for molecular dynamics simulations. *J. Phys. Chem.* **95,** 3358–3363 (1991).

23. Demiralp, E., Çağin, T. & Goddard, W. A. Morse Stretch Potential Charge Equilibrium Force Field for Ceramics: Application to the Quartz-Stishovite Phase Transition and to Silica Glass. *Phys. Rev. Lett.* **82,** 1708–1711 (1999).

24. Kieu, L.-H., Delaye, J.-M., Cormier, L. & Stolz, C. Development of empirical potentials for sodium borosilicate glass systems. *J. Non-Cryst. Solids* **357,** 3313–3321 (2011).

25. Bauchy, M. Structural, vibrational, and elastic properties of a calcium aluminosilicate glass from molecular dynamics simulations: The role of the potential. *J. Chem. Phys.* **141,** 024507 (2014).

26. Phillips, J. C. Topology of covalent non-crystalline solids I: Short-range order in chalcogenide alloys. *J. Non-Cryst. Solids* **34,** 153–181 (1979).

27. Bauchy, M., Guillot, B., Micoulaut, M. & Sator, N. Viscosity and viscosity anomalies of model silicates and magmas: A numerical investigation. *Chem. Geol.* **346,** 47–56 (2013).

28. Plimpton, S. Fast Parallel Algorithms for Short-Range Molecular Dynamics. *J. Comput. Phys.* **117,** 1–19 (1995).

29. Vollmayr, K., Kob, W. & Binder, K. Cooling-rate effects in amorphous silica: A computer-simulation study. *Phys. Rev. B* **54,** 15808–15827 (1996).

30. Tangney, P. & Scandolo, S. An ab initio parametrized interatomic force field for silica. *J. Chem. Phys.* **117,** 8898–8904 (2002).

31. Yuan, F. & Huang, L. Molecular dynamics simulation of amorphous silica under uniaxial tension: From bulk to nanowire. *J. Non-Cryst. Solids* **358,** 3481–3487 (2012).

32. Roder, A., Kob, W. & Binder, K. Structure and dynamics of amorphous silica surfaces. *J. Chem. Phys.* **114,** 7602–7614 (2001).

33. Yuan, F. & Huang, L. Brittle to Ductile Transition in Densified Silica Glass. *Sci. Rep.* **4,** (2014).

34. Bauchy, M. Structural, vibrational, and elastic properties of a calcium aluminosilicate glass from molecular dynamics simulations: The role of the potential. *J. Chem. Phys.* **141,** 024507 (2014).

35. Pedone, A., Malavasi, G., Cormack, A. N., Segre, U. & Menziani, M. C. Insight into Elastic Properties of Binary Alkali Silicate Glasses; Prediction and Interpretation through Atomistic Simulation Techniques. *Chem. Mater.* **19,** 3144–3154 (2007).

36. Lane, J. M. D. Cooling rate and stress relaxation in silica melts and glasses via microsecond molecular dynamics. *Phys. Rev. E* **92,** 012320 (2015).

37. Grimley, D. I., Wright, A. C. & Sinclair, R. N. Neutron scattering from vitreous silica IV. Time-of-flight diffraction. *J. Non-Cryst. Solids* **119,** 49–64 (1990).

38. Wright, A. C. Neutron and X-ray amorphography. *J. Non-Cryst. Solids* **106,** 1–16 (1988).

39. Lorch, E. Neutron diffraction by germania, silica and radiation-damaged silica glasses. *J. Phys. C Solid State Phys.* **2,** 229 (1969).

40. Mazurin, O. V., Streltsina, M. V. & Shvaiko-Shvaikovskaya, T. P. Handbook of glass data, Part A. *Silica Glass Bin. Silic. Glas.* (1983).

41. Pilla, O., Angelani, L., Fontana, A., Gonçalves, J. R. & Ruocco, G. Structural and dynamical consequences of density variation in vitreous silica. *J. Phys. Condens. Matter* **15,** S995 (2003).

42. Wright, A. C. The comparison of molecular dynamics simulations with diffraction experiments. *J. Non-Cryst. Solids* **159,** 264–268 (1993).

43. Henderson, G. S. A Si K-edge EXAFS/XANES study of sodium silicate glasses. *J. Non-Cryst. Solids* **183,** 43–50 (1995).

44. Poulsen, H. HF Poulsen, J. Neuefeind, H.-B. Neumann, JR Schneider, MD Zeidler. *J Non-Cryst Solids* **188,** 63 (1995).

45. Pettifer, R. F., Dupree, R., Farnan, I. & Sternberg, U. NMR determinations of Si 薄 O 薄 Si bond angle distributions in silica. *J. Non-Cryst. Solids* **106,** 408–412 (1988).

46. Mozzi, R. L. & Warren, B. E. The structure of vitreous silica. *J. Appl. Crystallogr.* **2,** 164–172 (1969).

47. Mauri, F., Pasquarello, A., Pfrommer, B. G., Yoon, Y.-G. & Louie, S. G. Si-O-Si bond-angle distribution in vitreous silica from first-principles ${}^{29}\mathrm{Si}$ NMR analysis. *Phys. Rev. B* **62,** R4786–R4789 (2000).

48. O'Keeffe, M. & Hyde, B. G. On Si—O—Si configurations in silicates. *Acta Crystallogr. Sect. B* **34,** 27–32 (1978).

49. Van Ginhoven, R. M., Jónsson, H. & Corrales, L. R. Silica glass structure generation for \textit{ab initio} calculations using small samples of amorphous silica. *Phys. Rev. B* **71,** 024208 (2005).

50. Muralidharan, K., Simmons, J. H., Deymier, P. A. & Runge, K. Molecular dynamics studies of brittle fracture in vitreous silica: Review and recent progress. *J. Non-Cryst. Solids* **351,** 1532–1542 (2005).

51. Bansal, N. P. & Doremus, R. H. *Handbook of Glass Properties*. (Elsevier, 2013).

52. Jr, J. C. M. Self-diffusivity of network oxygen in vitreous SiO2. *Appl. Phys. Lett.* **45,** 1187–1189 (1984).

53. Bauchy, M. & Micoulaut, M. From pockets to channels: Density-controlled diffusion in sodium silicates. *Phys. Rev. B* **83,** 184118 (2011).

54. Bauchy, M., Guillot, B., Micoulaut, M. & Sator, N. Viscosity and viscosity anomalies of model silicates and magmas: A numerical investigation. *Chem. Geol.* **346,** 47–56 (2013).

55. Koudriachova, M. V., Beckers, J. V. L. & de Leeuw, S. W. Computer simulation of the quartz surface: a combined ab initio and empirical potential approach. *Comput. Mater. Sci.* **20,** 381–386 (2001).

56. Benoit, M., Ispas, S., Jund, P. & Jullien, R. Model of silica glass from combined classical and ab initio molecular-dynamics simulations. *Eur. Phys. J. B - Condens. Matter Complex Syst.* **13,** 631–636 (2000).

57. Cormack, A. N., Du, J. & Zeitler, T. R. Sodium ion migration mechanisms in silicate glasses probed by molecular dynamics simulations. *J. Non-Cryst. Solids* **323,** 147–154 (2003).

58. Wang, B., Yu, Y., Lee, Y. J. & Bauchy, M. Intrinsic Nano-Ductility of Glasses: The Critical Role of Composition. *Front. Mater.* **2,** (2015).

59. Wang, B., Yu, Y., Wang, M., Mauro, J. C. & Bauchy, M. Nanoductility in silicate glasses is driven by topological heterogeneity. *Phys. Rev. B* **93,** 064202 (2016).

60. Du, J. & Cormack, A. N. The medium range structure of sodium silicate glasses: a molecular dynamics simulation. *J. Non-Cryst. Solids* **349,** 66–79 (2004).

61. Wright, A. C. *et al.* Neutron diffraction studies of silicate glasses. *Toledo OH USA Juillet* 64 (1991).

62. Misawa, M., Price, D. L. & Suzuki, K. The short-range structure of alkali disilicate glasses by pulsed neutron total scattering. *J. Non-Cryst. Solids* **37,** 85–97 (1980).

63. Grandinetti, P. J. *et al.* Solid-State 17O Magic-Angle and Dynamic-Angle Spinning NMR Study of the SiO2 Polymorph Coesite. *J. Phys. Chem.* **99,** 12341–12348 (1995).

64. Yu, Y., Wang, B., Wang, M., Sant, G. & Bauchy, M. Revisiting Silica with ReaxFF: Towards Improved Predictions of Glass Structure and Properties via Reactive Molecular Dynamics. *Non-Cryst. Solids*

65. Greaves, G. N., Fontaine, A., Lagarde, P., Raoux, D. & Gurman, S. J. Local structure of silicate glasses. *Nature* **293,** 611–616 (1981).

66. Maekawa, H., Maekawa, T., Kawamura, K. & Yokokawa, T. The structural groups of alkali silicate glasses determined from 29Si MAS-NMR. *J. Non-Cryst. Solids* **127,** 53–64 (1991).

67. Pettifer, R. F., Dupree, R., Farnan, I. & Sternberg, U. NMR determinations of Si 薄 O 薄 Si bond angle distributions in silica. *J. Non-Cryst. Solids* **106,** 408–412 (1988).

68. Farnan, I. *et al.* Quantification of the disorder in network-modified silicate glasses. *Nature* **358,** 31–35 (1992).

69. Bauchy, M., Qomi, M. J. A., Bichara, C., Ulm, F.-J. & Pellenq, R. J.-M. Rigidity Transition in Materials: Hardness is Driven by Weak Atomic Constraints. *Phys. Rev. Lett.* **114,** 125502 (2015).

70. Bauchy, M. & Micoulaut, M. Densified network glasses and liquids with thermodynamically reversible and structurally adaptive behaviour. *Nat. Commun.* **6,** (2015).

71. Bauchy, M. & Micoulaut, M. Atomic scale foundation of temperature-dependent bonding constraints in network glasses and liquids. *J. Non-Cryst. Solids* **357,** 2530–2537 (2011).

72. Bauchy, M. *et al.* Angular rigidity in tetrahedral network glasses with changing composition. *Phys. Rev. B* **84,** 054201 (2011).

73. Ojwang, J. G. O., van Santen, R., Kramer, G. J., van Duin, A. C. & Goddard III, W. A. Modeling of hydrogen Storage materials: a reactive Force field for NaH. (2008).

74. Shelby, J. E. Viscosity and thermal expansion of lithium aluminosilicate glasses. *J. Appl. Phys.* **49,** 5885–5891 (1978).

75. Lin, C.-C., Shen, P., Chang, H. M. & Yang, Y. J. Composition dependent structure and elasticity of lithium silicate glasses: Effect of ZrO2 additive and the combination of alkali silicate glasses. *J. Eur. Ceram. Soc.* **26,** 3613–3620 (2006).

76. Mauro, J. C. & Zanotto, E. D. Two Centuries of Glass Research: Historical Trends, Current Status, and Grand Challenges for the Future. *Int. J. Appl. Glass Sci.* **5,** 313–327 (2014).

77. Mauro, J. C. Grand challenges in glass science. *Fontiers Mater.* **1,** 20 (2014).

78. Mauro, J. C., Philip, C. S., Vaughn, D. J. & Pambianchi, M. S. Glass Science in the United States: Current Status and Future Directions. *Int. J. Appl. Glass Sci.* **5,** 2–15 (2014).

79. Phillips, J. C. Topology of covalent non-crystalline solids .1. Short-range order in chalcogenide alloys. *J. Non-Cryst. Solids* **34,** 153–181 (1979).

80. Phillips, J. C. Topology of covalent non-crystalline solids II: Medium-range order in chalcogenide alloys and As-Si-Ge. *J. Non-Cryst. Solids* **43,** 37–77 (1981).

81. Mauro, J. C. Topological constraint theory of glass. *Am. Ceram. Soc. Bull.* **90,** 31–37 (2011).

82. Bauchy, M. Topological constraints and rigidity of network glasses from molecular dynamics simulations. *Am. Ceram. Soc. Bull.* **91,** 34–38A (2012).

83. Bauchy, M. & Micoulaut, M. Atomic scale foundation of temperature-dependent bonding constraints in network glasses and liquids. *J. Non-Cryst. Solids* **357,** 2530–2537 (2011).

84. Bauchy, M. *et al.* Angular rigidity in tetrahedral network glasses with changing composition. *Phys. Rev. B* **84,** 054201 (2011).

85. Maxwell, J. C. L. On the calculation of the equilibrium and stiffness of frames. *Philos. Mag. Ser. 4* **27,** 294–299 (1864).

86. Pignatelli, I., Kumar, A., Bauchy, M. & Sant, G. Topological Control on Silicates' Dissolution Kinetics. *Langmuir* **32,** 4434–4439 (2016).

87. Oey, T. *et al.* An improved basis for characterizing the suitability of fly ash as a cement replacement agent. *J. Am. Ceram. Soc.* (2017). doi:10.1111/jace.14974

88. Oey, T. *et al.* Topological controls on the dissolution kinetics of glassy aluminosilicates. *J. Am. Ceram. Soc.* n/a–n/a doi:10.1111/jace.15122

89. Mascaraque, N., Bauchy, M. & Smedskjaer, M. M. Correlating the Network Topology of Oxide Glasses with their Chemical Durability. *J. Phys. Chem. B* **121,** 1139–1147 (2017).

90. Mascaraque, N. *et al.* Dissolution Kinetics of Hot Compressed Oxide Glasses. *J. Phys. Chem. B* **121,** 9063–9072 (2017).

91. Pignatelli, I. *et al.* A dissolution-precipitation mechanism is at the origin of concrete creep in moist environments. *J. Chem. Phys.* **145,** 054701 (2016).

92. Bauchy, M. Nanoengineering of concrete via topological constraint theory. *MRS Bull.* **42,** 50–54 (2017).

93. Pignatelli, I. *et al.* Direct Experimental Evidence for Differing Reactivity Alterations of Minerals following Irradiation: The Case of Calcite and Quartz. *Sci. Rep.* **6,** 20155 (2016).

94. Hsiao, Y.-H. *et al.* Effects of Irradiation on Albite's Chemical Durability. *J. Phys. Chem. A* **121,** 7835–7845 (2017).

95. Bauchy, M. Structural, vibrational, and elastic properties of a calcium aluminosilicate glass from molecular dynamics simulations: The role of the potential. *J. Chem. Phys.* **141,** 024507 (2014).

96. Yu, Y., Wang, B., Wang, M., Sant, G. & Bauchy, M. Revisiting silica with ReaxFF: Towards improved predictions of glass structure and properties via reactive molecular dynamics. *J. Non-Cryst. Solids* **443,** 148–154 (2016).

97. Krishnan, N. M. A. *et al.* Enthalpy landscape dictates the irradiation-induced disordering of quartz. *Phys Rev X* (2017).

98. Krishnan, N. M. A., Wang, B., Le Pape, Y., Sant, G. & Bauchy, M. Irradiation- vs. vitrification-induced disordering: The case of α-quartz and glassy silica. *J. Chem. Phys.* **146,** 204502 (2017).

99. Li, X. *et al.* Cooling rate effects in sodium silicate glasses: Bridging the gap between molecular dynamics simulations and experiments. *J. Chem. Phys.* **147,** 074501 (2017).

100. Vollmayr, K., Kob, W. & Binder, K. Cooling-rate effects in amorphous silica: A computer-simulation study. *Phys. Rev. B* **54,** 15808–15827 (1996).

101. Lane, J. M. D. Cooling rate and stress relaxation in silica melts and glasses via microsecond molecular dynamics. *Phys. Rev. E* **92,** 012320 (2015).

102. Grimley, D. I., Wright, A. C. & Sinclair, R. N. Neutron scattering from vitreous silica IV. Time-of-flight diffraction. *J. Non-Cryst. Solids* **119,** 49–64 (1990).

103. Yeon, J. & van Duin, A. C. T. ReaxFF Molecular Dynamics Simulations of Hydroxylation Kinetics for Amorphous and Nano-Silica Structure, and Its Relations with Atomic Strain Energy. *J. Phys. Chem. C* **120,** 305–317 (2016).

104. D'Souza, A. S. & Pantano, C. G. Mechanisms for Silanol Formation on Amorphous Silica Fracture Surfaces. *J. Am. Ceram. Soc.* **82,** 1289–1293 (1999).

105. Burneau, A., Gallas, J. & Legrand, A. The surface properties of silicas. *Vib. Spectrosc. John Wiley Chichester* 147–234 (1998).

106. Bakaev, V. A. & Steele, W. A. On the computer simulation of a hydrophobic vitreous silica surface. *J. Chem. Phys.* **111,** 9803–9812 (1999).

107. Levine, S. M. & Garofalini, S. H. A structural analysis of the vitreous silica surface via a molecular dynamics computer simulation. *J. Chem. Phys.* **86,** 2997–3002 (1987).

108. Siboulet, B., Coasne, B., Dufrêche, J.-F. & Turq, P. Hydrophobic Transition in Porous Amorphous Silica. *J. Phys. Chem. B* **115,** 7881–7886 (2011).

109. Wiederhorn, S. M. Fracture Surface Energy of Glass. *J. Am. Ceram. Soc.* **52,** 99–105 (1969).

110. Shchipalov, Y. K. Surface Energy of Crystalline and Vitreous Silica. *Glass Ceram.* **57,** 374–377 (2000).

111. Mizele, J., Dandurand, J. L. & Schott, J. Determination of the surface energy of amorphous silica from solubility measurements in micropores. *Surf. Sci.* **162,** 830–837 (1985).

112. Feuston, B. P. & Garofalini, S. H. Water-induced relaxation of the vitreous silica surface. *J. Appl. Phys.* **68,** 4830–4836 (1990).

113. Garofalini, S. H. Molecular dynamics computer simulations of silica surface structure and adsorption of water molecules. *J. Non-Cryst. Solids* **120,** 1–12 (1990).

114. Fogarty, J. C., Aktulga, H. M., Grama, A. Y., van Duin, A. C. T. & Pandit, S. A. A reactive molecular dynamics simulation of the silica-water interface. *J. Chem. Phys.* **132,** 174704 (2010).

115. Rimsza, J. M., Yeon, J., van Duin, A. C. T. & Du, J. Water Interactions with Nanoporous Silica: Comparison of ReaxFF and ab Initio based Molecular Dynamics Simulations. *J. Phys. Chem. C* **120,** 24803–24816 (2016).

116. Mueller, R., Kammler, H. K., Wegner, K. & Pratsinis, S. E. OH surface density of SiO2 and TiO2 by thermogravimetric analysis. *Langmuir* **19,** 160–165 (2003).

117. Zhuravlev, L. T. Concentration of hydroxyl groups on the surface of amorphous silicas. *Langmuir* **3,** 316–318 (1987).

118. Zhuravlev, L. T. The surface chemistry of amorphous silica. Zhuravlev model. *Colloids Surf. Physicochem. Eng. Asp.* **173,** 1–38 (2000).

119. Du, J. & Cormack, A. N. Molecular Dynamics Simulation of the Structure and Hydroxylation of Silica Glass Surfaces. *J. Am. Ceram. Soc.* **88,** 2532–2539 (2005).

120. Gregg, S. & Sing, K. S. Adsorption, surface area, and porosity. (1983).

121. Ori, G., Massobrio, C., Bouzid, A. & Coasne, B. Molecular Modeling of Glassy Surfaces. in *Molecular Dynamics Simulations of Disordered Materials* 345–365 (Springer, Cham, 2015).

122. Bolis, V., Fubini, B., Marchese, L., Martra, G. & Costa, D. Hydrophilic and hydrophobic sites on dehydrated crystalline and amorphous silicas. *J. Chem. Soc. Faraday Trans.* **87,** 497–505 (1991).

123. Bauchy, M., Qomi, M. J. A., Bichara, C., Ulm, F.-J. & Pellenq, R. J.-M. Rigidity Transition in Materials: Hardness is Driven by Weak Atomic Constraints. *Phys. Rev. Lett.* **114,** 125502 (2015).

124. Wang, M. *et al.* Crucial effect of angular flexibility on the fracture toughness and nano-ductility of aluminosilicate glasses. *J. Non-Cryst. Solids* **454,** 46–51 (2016).

125. Zhang, M. & Boolchand, P. The Central Role of Broken Bond-Bending Constraints in Promoting Glass Formation in the Oxides. *Science* **266,** 1355–1357 (1994).

126. Boolchand, P. & Thorpe, M. F. Glass-Forming Tendency, Percolation of Rigidity, and Onefold-Coordinated Atoms in Covalent Networks. *Phys. Rev. B* **50,** 10366–10368 (1994).

127. Boolchand, P., Zhang, M. & Goodman, B. Influence of one-fold-coordinated atoms on mechanical properties of covalent networks. *Phys. Rev. B* **53,** 11488–11494 (1996).

128. Ganneau, F. P., Constantinides, G. & Ulm, F.-J. dual-indentation technique for the assessment of strength properties of cohesive-frictional materials. *Int. J. Solids Struct.* **43,** 1727–1745 (2006).

129. Kjeldsen, J., Smedskjaer, M. M., Mauro, J. C. & Yue, Y. Hardness and incipient plasticity in silicate glasses: Origin of the mixed modifier effect. *Appl. Phys. Lett.* **104,** 051913 (2014).

130. Pedone, A. *et al.* A new self-consistent empirical interatomic potential model for oxides, silicates, and silica-based glasses. *J. Phys. Chem. B* **110,** 11780 (2006).

131. Luo, J., Vargheese, K. D., Tandia, A., Hu, G. & Mauro, J. C. Crack nucleation criterion and its application to impact indentation in glasses. *Sci. Rep.* **6,** (2016).

132. Bauchy, M. Structural, vibrational, and thermal properties of densified silicates: Insights from molecular dynamics. *J. Chem. Phys.* **137,** 044510 (2012).

133. Li, X. *et al.* Cooling-Rate Effects in Sodium Silicate Glasses: Bridging the Gap between Molecular Dynamics Simulations and Experiments. *ArXiv170408209 Cond-Mat* (2017).

134. Bauchy, M. Structural, vibrational, and elastic properties of a calcium aluminosilicate glass from molecular dynamics simulations: The role of the potential. *J. Chem. Phys.* **141,** 024507 (2014).

135. Qomi, M. A. *et al.* Combinatorial molecular optimization of cement hydrates. *Nat. Commun.* **5,** (2014).

136. Bauchy, M., Qomi, M. J. A., Bichara, C., Ulm, F.-J. & Pellenq, R. J.-M. Rigidity Transition in Materials: Hardness is Driven by Weak Atomic Constraints. *Phys. Rev. Lett.* **114,** 125502 (2015).

137. Ganneau, F. P., Constantinides, G. & Ulm, F.-J. Dual-indentation technique for the assessment of strength properties of cohesive-frictional materials. *Int. J. Solids Struct.* **43,** 1727–1745 (2006).

138. Li, X. *et al.* Cooling-Rate Effects in Sodium Silicate Glasses: Bridging the Gap between Molecular Dynamics Simulations and Experiments. *ArXiv170408209 Cond-Mat* (2017).

139. General formulation of pressure and stress tensor for arbitrary many-body interaction potentials under periodic boundary conditions. *J. Chem. Phys.* **131,** 154107 (2009).

140. Hardness and incipient plasticity in silicate glasses: Origin of the mixed modifier effect. *Appl. Phys. Lett.* **104,** 051913 (2014).

141. Kjeldsen, J., Smedskjaer, M. M., Mauro, J. C. & Yue, Y. On the origin of the mixed alkali effect on indentation in silicate glasses. *J. Non-Cryst. Solids* **406,** 22–26 (2014).

142. Aakermann, K. G. *et al.* Indentation deformation mechanism of isostatically compressed mixed alkali aluminosilicate glasses. *J. Non-Cryst. Solids* **426,** 175–183 (2015).

143. Luo, J. *et al.* Competing Indentation Deformation Mechanisms in Glass Using Different Strengthening Methods. *Front. Mater.* **3,** (2016).

144. Möbius, R. & Heussinger, C. (Ir)reversibility in dense granular systems driven by oscillating forces. *Soft Matter* **10,** 4806 (2014).

145. Yu, Y., Krishnan, A. N., Smedskjaer, M. M., Mauro, J. C. & Bauchy, M. Origin of the Mixed Alkaline Earth Effect on the Hardness of Silicate Glasses. in *12th Pacific Rim Conference on Ceramic and Glass Technology* (2017).

146. Varshneya, A. K. *Fundamentals of inorganic glasses*. (Elsevier, 2013).

147. Bauchy, M. *et al.* Topological Control on Atomic Networks' Relaxation Under Stress. *ArXiv160505043 Cond-Mat* (2016).

148. Yu, Y. *et al.* Stretched Exponential Relaxation of Glasses at Low Temperature. *Phys. Rev. Lett.* **115,** 165901 (2015).

149. Gao, Y. & Cramer, C. Mixed cation effects in glasses with three types of alkali ions. *Solid State Ion.* **176,** 2279–2284 (2005).

150. Smedskjaer, M. M. *et al.* Topological Principles of Borosilicate Glass Chemistry. *J. Phys. Chem. B* **115,** 12930–12946 (2011).

151. Cormack, A. N., Du, J. & Zeitler, T. R. Alkali ion migration mechanisms in silicate glasses probed by molecular dynamics simulations. *Phys Chem Chem Phys* **4,** 3193–3197 (2002).

152. Bauchy, M. Structural, vibrational, and thermal properties of densified silicates: Insights from molecular dynamics. *J. Chem. Phys.* **137,** 044510 (2012).

153. Bauchy, M., Guillot, B., Micoulaut, M. & Sator, N. Viscosity and viscosity anomalies of model silicates and magmas: A numerical investigation. *Chem. Geol.* **346,** 47–56 (2013).

154. Welch, R. *et al.* Dynamics of Glass Relaxation at Room Temperature. *Phys. Rev. Lett.* **110,** 265901 (2013).

155. Yu, Y. *et al.* Stretched Exponential Relaxation of Glasses at Low Temperature. *Phys. Rev. Lett.* **115,** 165901 (2015).

156. Richard, P., Nicodemi, M., Delannay, R., Ribière, P. & Bideau, D. Slow relaxation and compaction of granular systems. *Nat. Mater.* **4,** 121–128 (2005).

157. Lacks, D. J. & Osborne, M. J. Energy Landscape Picture of Overaging and Rejuvenation in a Sheared Glass. *Phys. Rev. Lett.* **93,** 255501 (2004).

158. Phillips, J. C. Stretched exponential relaxation in molecular and electronic glasses. *Rep. Prog. Phys.* **59,** 1133 (1996).

159. Thompson, A. P., Plimpton, S. J. & Mattson, W. General formulation of pressure and stress tensor for arbitrary many-body interaction potentials under periodic boundary conditions. *J. Chem. Phys.* **131,** 154107 (2009).

160. Yu, Y. *et al.* Stretched Exponential Relaxation of Glasses at Low Temperature. *Phys. Rev. Lett.* **115,** 165901 (2015).